

Capacitive lithium capture system using a mixed LiMn_2O_4 and LiAlO_2 material

Tasneem Elmakki^a, Sifani Zavahir^a, Ho Kyong Shon^b, Guillermo Hijós Gago^c, Hyunwoong Park^d, Dong Suk Han^{a,e,*}

^a Center for Advanced Materials, Qatar University, P.O. Box 2713, Doha, Qatar

^b ARC Research Hub for Nutrients in a Circular Economy, Center for Technology in Water and Wastewater, School of Civil and Environmental Engineering, Faculty of Engineering and IT, University of Technology Sydney, P.O. Box 123, Broadway, NSW 2007, Australia

^c O&M Desalination Middle East and Oceania, Acciona Agua, P.O. Box 55976, Doha, Qatar

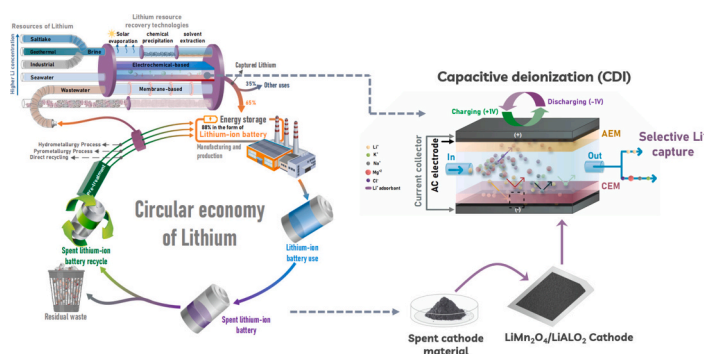
^d School of Energy Engineering, Kyunpook National University, Daegu 41566, Republic of Korea

^e Department of Chemical Engineering, College of Engineering, Qatar University, P.O. Box 2713, Doha, Qatar

HIGHLIGHTS

- LMO/LAO (90/10) cathodes reached highest specific capacitance: 159.6 F/g.
- MCDI system with LMO/LAO electrode peaked at 900 $\mu\text{mol/g}$ Li adsorption.
- Mixed electrode improved Li recovery efficiency by 146 %.
- Demonstrated high Li selectivity over competing ions, including Mg^{2+} .
- Maintained low energy consumption at 0.67 kWh/m^3 .

GRAPHICAL ABSTRACT



ARTICLE INFO

Keywords:

Lithium recovery
Membrane-based capacitive deionization (MCDI)
Spent Li-ion batteries
Circular economy
 LiMn_2O_4 (LMO)

ABSTRACT

The increasing demand for lithium (Li), a crucial material in various industries, requires efficient recovery methods and a shift toward a circular economy. This study investigates a fast, eco-friendly technique for selective Li recovery, emphasizing the use of innovative materials from spent Li-ion batteries (SLIBs), particularly LiMn_2O_4 (LMO)/ LiAlO_2 (LAO)-based materials, to enhance Li's circular economy. Conventional Li recovery methods typically involve prolonged processes with chemical additives and environmental concerns, whereas electrochemical systems like membrane-based capacitive deionization (MCDI) offer promising high removal capacities, regeneration ability, and scalability. However, no commercial electrochemical Li recovery system underscores the need for continued research to improve their performance. This study employs MCDI for selective Li recovery, examining various electrode materials, including commercial activated carbon, LMO-based electrodes, and modified LMO/LAO-based electrodes. The mixed LiMn_2O_4 / LiAlO_2 cathode exhibited high selectivity for Li^+ extraction with a recovery efficiency of 83.1 %, achieving a deionization capacity of 38.15 mg/g at 1.0 V under an initial feed concentration of 5 mM LiCl. The Li^+ adsorption reached 900 $\mu\text{mol/g}$, with a separation factor

* Corresponding author.

E-mail address: dhan@qu.edu.qa (D.S. Han).

<https://doi.org/10.1016/j.desal.2024.118195>

Received 21 June 2024; Received in revised form 6 October 2024; Accepted 11 October 2024

Available online 21 October 2024

0011-9164/© 2024 The Authors. Published by Elsevier B.V. This is an open access article under the CC BY license (<http://creativecommons.org/licenses/by/4.0/>).

($\alpha_{Mg^{2+}}^{Li^+}$) of 3.77 ($C_{Mg^{2+}}^+/C_{Li^+}^+ = 1$), setting a robust foundation for a comprehensive Li recovery framework that meets the increasing Li demand while minimizing environmental impact.

1. Introduction

The surging demand for lithium (Li) as an essential component in various industries, such as polymer production, electronics, energy storage, ceramics, and lubricants, drives the need for efficient recovery methods and a circular economy approach. As of 2016, 35 % of the global Li supply was allocated to battery manufacturing, emphasizing Li's importance in emerging technologies [1]. The demand for Li-ion batteries (LIBs) is projected to reach 25,000 tons annually, necessitating innovative recovery strategies. Li resources include both liquid (brines, seawater, wastewater) and solid (mineral ores) forms, with liquid reserves constituting 85 % of the accessible extractable Li, totaling 1.6 M tons [2]. The global Li content in oceans is approximately 2.5×10^{14} kg, featuring an average concentration of 0.17 mg/L [3]. Among liquid sources, high-salinity brines show the highest Li concentrations, with geothermal brines reaching up to 15 mg/L, while Salt Lake brines exhibit significantly higher concentrations of 1000–3000 mg/L [3]. Given the extensive use and consumption of Li, it is imperative to focus on its efficient recovery from all viable sources using extraction technologies that are both effective and environmentally benign.

Various technologies have been employed to address the imbalance in Li supply and demand, including solar evaporation, chemical precipitation, and solvent extraction. These methods, however, are associated with long processing times, the need for chemical additives, and environmental impacts. In response, innovative Li recovery technologies are being exploited, including ionic exchange [4], molecular sieve adsorption [5,6], various membrane techniques [7,8], and electrochemical recovery methods [9,10]. Electrochemical systems are particularly promising for Li recovery due to their unlimited removal capacities and scalability. These systems are noted for their superior Li recovery capacities, selectivity, cyclic efficiency, reversibility, and tunability [11]. Li capture in these systems is primarily facilitated by applying a current, with the immobilization rate directly proportional to the charge invested in the electrodes [12].

A notable innovation in this field is the membrane-based capacitive deionization (MCDI) process, originally utilized in low-salinity water desalination, where about 1–1.3 V is applied to capacitive electrodes to

desalinate the feed solution effectively. With the shift toward Li recovery, the principle of battery operation has been adapted to enhance the MCDI's application in Li extraction. This adaptation involves the integration of a faradaic intercalating electrode with anion (AEM) and cation exchange membranes (CEM). This configuration allows for the selective migration and capture of Li ions: Li ions pass through the CEM and are absorbed by the intercalating electrode, while anions traverse an AEM and accumulate at the capacitive electrode.

Shi et al. [13] were pioneers in employing MCDI for Li recovery, utilizing a monovalent selective CEM to selectively capture Li from solutions containing both Li^+ and Mg^{2+} . Their initial efforts achieved a Li removal rate of 38 %, with a selectivity coefficient of 2.95 against Mg. Further advancements in the CDI technology emphasized Li selectivity, integrating faradaic Li-specific intercalation electrodes that often replaced one of the traditional porous carbon electrodes, evolving into what is known as hybrid capacitive deionization (HCDI). Recent developments in HCDI systems designed for Li recovery have seen extensive experimentation with various battery-based faradaic intercalation electrodes, including $LiMn_2O_4$ (LMO) [14–19], $LiO-FeO-Mn_2O_3$ [20], $Li-Mn-Ti-O$ [3,21–23], $LiNi_{0.038}Mo_{0.012}Mn_{1.95}O_4$ (LNMMO) [24], $LiVO_4$ (LVO) [25], and $LiCoMnO_4$ [26]. Research, as summarized in Table 1, has predominantly focused on developing electrodes, particularly those based on LMO, whether in their pristine form or modified. Despite these advancements, research on CDI and MCDI technologies for Li recovery remains relatively limited. Thus, further research is necessary to explore the impact of feed solution characteristics, optimize current density, and identify more efficient electrode pairs.

Building on previous studies, LMO emerges as a prominent Li intercalation material for CDI applications due to its robust redox properties and significant theoretical adsorption capacity. However, its utility is somewhat curtailed by issues related to conductivity and stability. To mitigate these challenges, this study proposes the incorporation of $LiAlO_2$ (LAO) to enhance LMO's performance. Commonly utilized as a conductive coating in commercially available LIBs, LAO features excellent Li^+ conductivity ($3 \times 10^{-5} /\Omega \text{ cm}$), a high Li^+ diffusion coefficient ($2.8 \times 10^{-11} \text{ m}^2/\text{s}$), and stable electrochemical properties over a wide voltage range [27]. The integration of LAO is expected to

Table 1
Summary of studies on CDI for selective Li recovery.

Research focus	Active cathode material	Experimental conditions				SAC (mg/g)	Ref.
		Initial salt conc. (mM)	Flow rate (ml/min)	Cell voltage (V)	Operation mode		
Process enhancement	AC	3.5996	10–30	0.6–1.4		–	[13]
		10	1	1		–	[18]
	LMO	34.37	20	1		2.415	[14]
		2.5	40	3.5		8.7	[15]
		2	20	0.1–2.0		1.36	[16]
		10	67	1.23		98	[20]
	CF-LNMMO	23.48	1	0.2–0.9	Contin.	14.4	[24]
	LNMO	5	10	1		1.66	[21]
Electrode development	LMTO	2.45	6	2		4.8	[22]
	LVO/rGO	15	40	1.2		39.53	[25]
	MnO_2/rGO	10	10	0.9–0.7		25.47	[28]
	LMO/GO	10	10	15 mA/g		30.53	[29]
	LCMO	10	10	1		30.53	[26]
	CoP/Co ₃ O ₄	1.17	–	0.2–0.6		37	[30]
	LMO	20	–	1	Batch	159.49	[19]
	LMTO	Brine	67	2	Contin.	800	[3]
Process evaluation	Carbon slurry	2.3	3 to 9	1.2		–	[31]
	λ -MnO ₂ sieve	5–10	10	0.2–2.2	Flow	33.9	[17]
Membrane development	LMTO	20	67	1.23		30	[32]
	AC/ZIF-8-PDA	10	20	0.5–1.5	Contin.	3	[33]

enhance LMO's conductivity and intercalation/deintercalation efficiency, thereby improving its effectiveness as a Li intercalating electrode in CDI. Moreover, the widespread use of both materials in LIBs underscores their potential for repurposing spent LMO/LAO-based LIB cathode materials.

This study seeks to investigate novel and efficient electrodes for

elemental Li recovery, aiming to evaluate the feasibility of a comprehensive Li recovery and recycling system. This system is poised to advance Li's circular economy. In this context, a novel Li intercalating electrode, combining LiAlO_2 with LiMn_2O_4 , was fabricated and tested using a simulated spent Li-ion batteries (SLiBs) cathode material in an MCDI system for targeted Li extraction from liquid resources. This study

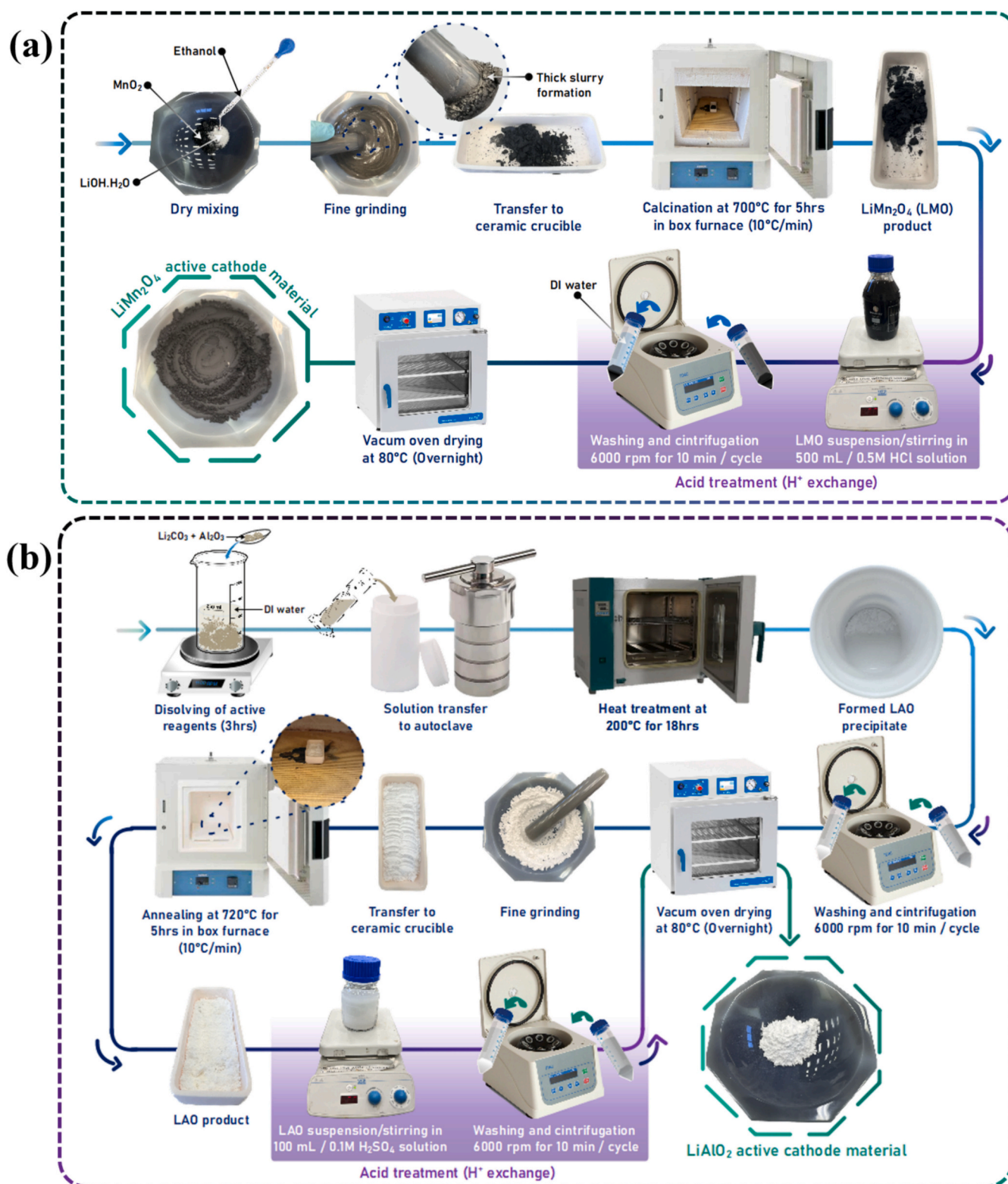


Fig. 1. Synthesis procedure for CDI electrode materials: (a) LiMn_2O_4 (LMO) synthesized using the solid-state reaction method. (b) LiAlO_2 (LAO) produced via the hydrothermal method.

is detailed through a graphical abstract that includes a schematic of the research methodology, along with depictions of various liquid Li sources and their respective capturing mechanisms with a circular Li-recovery framework.

2. Methodology

2.1. Chemicals and reagents

All chemicals used in this study were of analytical grade and used directly as received without any further purification. Lithium chloride (LiCl, $\geq 99.0\%$), lithium hydroxide monohydrate (LiOH·H₂O, 98.5 % - 101.5 %), lithium carbonate (LiCO₃, $\geq 99.0\%$), aluminum oxide (Al₂O₃), manganese(IV)-oxide (MnO₂, 85–90 %), poly(vinyl chloride) (PVC), tetrahydrofuran (THF, 99.9 %), sodium chloride (NaCl, 98.5 %), potassium chloride (KCl, 98.0 %), magnesium chloride (MgCl₂, 98.0 %), calcium chloride (CaCl₂, 90.0 %), and absolute ethanol were sourced from Sigma-Aldrich, located in St. Louis, MO, USA. Acetylene carbon was procured from MTI company in Richmond, California, USA. Sulfuric acid (H₂SO₄, 98 % solution) was from VWR Chemicals BDH (Leuven, Belgium), while hydrochloric acid (HCl, 35–38 %) was purchased from Research-lab fine chem industries in Mumbai, India. The feed solutions for the MCDI were prepared by dissolving these chemicals in deionized (DI) water, which was sourced from a Milli Q ultra-purification system (type 2) with a resistivity of 18.2 MΩ·cm.

2.2. Electrode fabrication

2.2.1. Synthesis of active materials

The active cathode material LiMn₂O₄ (LMO) was synthesized using the solid-state reaction method. Initially, LiOH·H₂O (1.2 g) and MnO₂ (4.8 g) were combined, dry-mixed, and ground with ethanol, then air-dried using a mortar and pestle. This mixture underwent calcination at 700 °C for 10 h in a box furnace (Nabertherm GmbH, Germany), heated at a rate of 10 °C/min. Following the calcination step, the resulting material was ground, and 2.5 g of it was then acid-treated with 0.5 M HCl overnight to extract Li-ion. The resulting precipitate was filtered, washed thrice with DI water, and centrifuged at 6000 rpm for 10 min each time. It was then dried overnight in a vacuum oven at 80 °C, producing Li-deficient LMO. The synthesis procedure is illustrated in Fig. 1a.

LiAlO₂ (LAO) was synthesized via the hydrothermal method. A mixture of Li₂CO₃ (3.69 g, 0.05 mol) and Al₂O₃ (5.09 g, 0.05 mol) was dissolved in 100 ml of DI water and stirred vigorously for 3 h. The solution was then transferred to a 500 ml Teflon liner and autoclaved at 200 °C for 18 h in a natural convection drying oven (Biobase, Biodustry). Upon cooling, the white LiAlO₂ precipitate was separated, washed three times with DI water, centrifuged at 6000 rpm for 10 min per cycle, and dried overnight at 80 °C in a vacuum oven. The dried precipitate was finely ground using a mortar and pestle, then annealed at 720 °C for 5 h in a ceramic crucible in a box furnace, with a heating rate of 10 °C/min to ensure phase purity and structural stability. Following this, the material was treated by suspending it in 100 ml of 0.1 M H₂SO₄ solution overnight with continuous stirring. After filtration, washing, and drying at 80 °C overnight, the active LAO product was obtained. The synthesis process for this material is illustrated in Fig. 1b.

2.2.2. Electrode preparation

For this investigation, electrodes were fabricated in two sizes: smaller electrodes measuring 3 × 2 cm² for electrochemical tests and larger ones at 6 × 6 cm² for evaluating performance in the MCDI cell. The electrode formulation consisted of a mass ratio of 8:1:1, comprising active electrode cathode material, acetylene carbon, and binder. This mixture was applied to a plain graphite sheet, serving as the substrate and current collector. The binder was prepared by dissolving PVC in THF. The components, including the active electrode material (LMO,

LAO, or their combination) and acetylene carbon, were blended and finely ground with a motor and pestle. This mixture was gradually integrated with the PVC/THF binder using a micropipette, ensuring uniformity through alternate magnetic stirring and ultrasonication in 30-min intervals for optimal mixing. The resulting homogeneous paste was then spread onto the graphite sheet and left to air-dry. The procedure was identical for the larger electrodes utilized in the MCDI setup, employing 360 mg of the active material. The specifics of the electrode compositions, including mass ratios used across various tests, are detailed in Table 2.

2.3. Material characterization

The crystalline structures of the samples were examined using X-ray diffraction (XRD) analysis, conducted on a PANalytical Empyrean X-ray diffractometer (XRD, PANalytical Empyrean, Malvern Analytical, Malvern, UK), equipped with a Cu Kα X-ray source (wavelength $\lambda = 1.5406 \text{ \AA}$) set to operate at 40 kV and 30 mA. To assess the morphological and structural distribution of the fabricated powders and electrodes, we employed scanning electron microscopy (SEM) equipped with an energy dispersive X-ray (EDX) spectroscopy (SEM/EDX, NOVANOSEM 450, FEI Company, Hillsboro, OR, USA) and transmission electron microscopy (TEM) using a FEI TECNAI G2 TEM, TF20. Additionally, the chemical composition of the electrodes was analyzed via X-ray photoelectron spectroscopy (XPS) using an AXIS Ultra DLD spectrometer.

2.4. Electrochemical characterization

The electrochemical properties of the fabricated electrodes were assessed using cyclic voltammetry (CV), galvanostatic charge/discharge (GCD), and electrochemical impedance spectroscopy (EIS), conducted on Gamry 5000 interface potentiostat (Gamry Instruments, Warminster, PA, USA) within a 1 M LiCl aqueous solution. The fabricated electrode functioned as the working electrode, with a Pt wire serving as the counter electrode and an Ag/AgCl (saturated KCl) used as the reference electrode. For EIS measurements, the frequency range was set from 0.01 Hz to 100 kHz, with an excitation signal amplitude of 5 mV vs. the open circuit voltage. In the GCD tests, a constant current of $\pm 0.1 \text{ A}$ was maintained, and voltage changes were recorded over a period of 1200 s. The specific capacitance was calculated from the GCD data using the following Eq. (1):

Table 2
Electrodes fabricated and tested in this study.

No.	Electrode naming	Weight ratio Active material: Acetylene Carbon: PVC (mg)	Active material LMO: LAO mass ratio	Electrode size
1	AC	Activated carbon	–	
2	LMO		100:0	
3	LMO/ LAO (90/10)		90:10	
4	LMO/ LAO (80/20)		80:20	
5	LMO/ LAO (50/50)	120 mg: 15 mg: 15 mg	50:50	3 × 2 cm
6	LMO/ LAO (20/80)		20:80	
7	LMO/ LAO (10/90)		10:90	
8	LAO		0:100	
9	AC-CDI	Activated carbon	–	
10	LMO-CDI		100:0	
11	LMO/ LAO- CDI	360 mg: 45 mg: 45 mg	90:10	6 × 6 cm

$$C = \frac{I \cdot \Delta t}{m \cdot \Delta V} \quad (1)$$

Here, C represents the specific capacitance (F/g), I is the discharge current, Δt is the time duration of the discharge in seconds, m denotes the mass of the active material in the electrode (g), and ΔV is the voltage (V) change during discharge.

2.5. Lithium extraction experiments in MCDI

2.5.1. Preparation of lab-scale MCDI unit

MCDI tests were performed using a bench-scale, flow-through system crafted in-house. The cell was assembled by stacking electrode sheets,

membranes, and a spacer sandwiched between two acrylic plates: each outfitted with two inlets and an outlet (1 cm in diameter) on the upper plate. These plates secured the electrodes and membranes, forming the cell structure. The cell's flow channel measured 6×6 cm, providing an effective ion adsorption/desorption area of 36 cm^2 .

During Li extraction tests, the working electrode functioned as the cathode to attract Li ions. The cathode coating on the graphite sheet was switched between different coatings: commercial activated carbon (AC-CDI) (Kuraray Chemical Co., Japan), LiMn_2O_4 (LMO-CDI), and a blend of $\text{LiMn}_2\text{O}_4/\text{LiAlO}_2$ (LMO/LAO-CDI). The anode consistently employed a commercial activated carbon-coated graphite sheet. CEMs and AEMs (ASTOM Corp., Japan) were positioned between the electrodes to filter out divalent ions. A non-conductive nylon spacer (200 μm) ensured

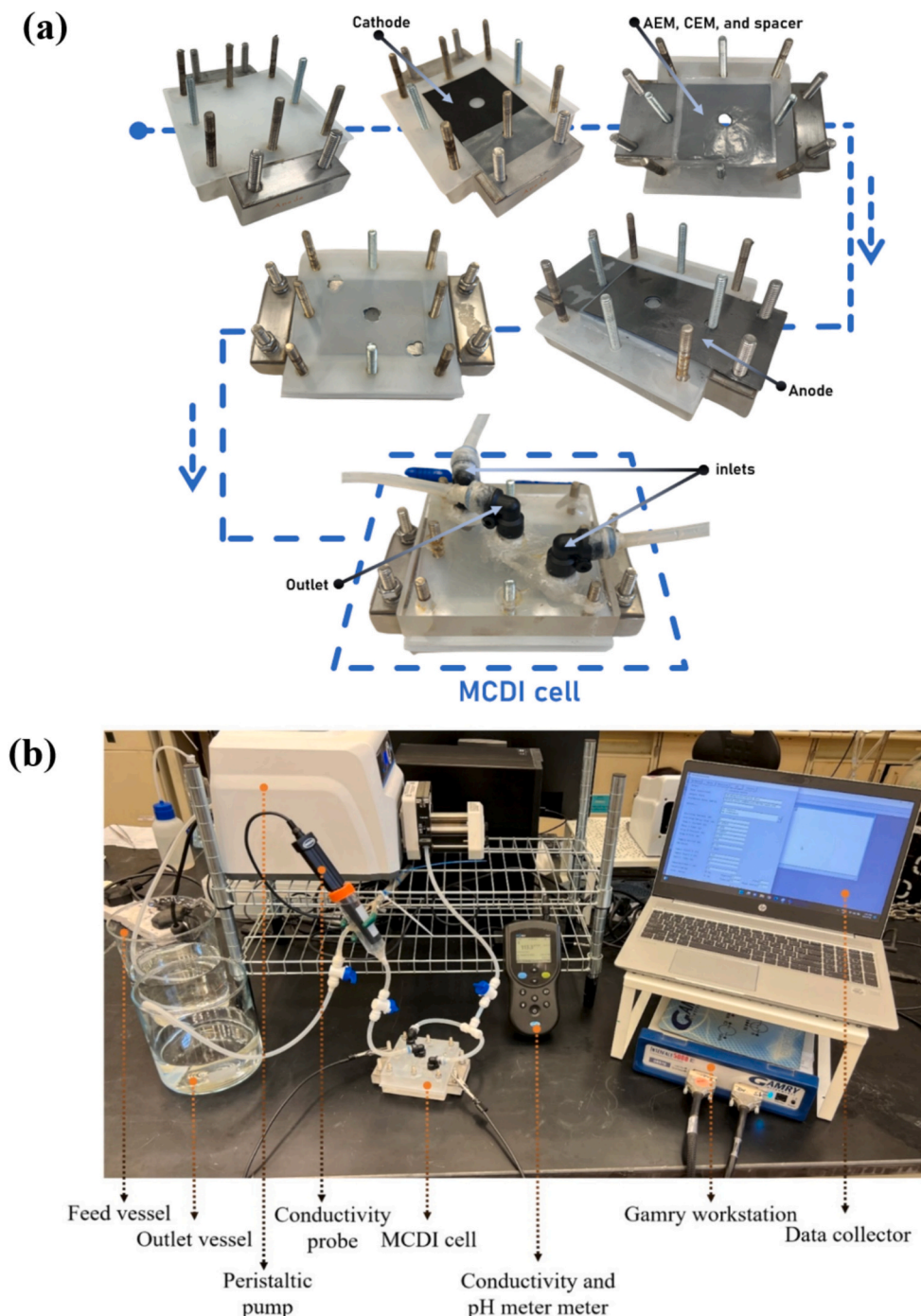


Fig. 2. Overview of MCDI components and setup: (a) Assembly and stacking of the MCDI cell. (b) Bench-scale experimental setup for MCDI testing.

separation of the membranes to prevent short-circuiting and facilitate fluid movement through the cell components. Fig. 2a and b show the assembled MCDI cell and the full bench-scale MCDI setup, respectively.

The MCDI system was connected to a feed vessel via two inlets and an outlet channel, circulating the feed through 3 mm diameter silicon tubing using a peristaltic pump (CARTRIDGE PUMP, Masterflex® L/S®, model 7519-06). At the outlet, a station facilitated sample collection and measurement of conductivity and pH with a conductivity/pH probe (HQ14D, Hach). The electrical potential across the MCDI cell was controlled using a potentiostat (Gamry 5000 interface). Experiments were conducted in continuous batch mode, cycling between the Li-containing solution and DI water for various charge/discharge cycles.

2.5.2. MCDI charge-discharge tests

Li extraction efficiency in the MCDI cell was assessed using the following procedure: Initially, 100 ml of a 5 mM LiCl solution was circulated at 30 rpm for 10 min using a peristaltic pump to establish a stable flow and ensure all components were thoroughly wetted. A 10 ml sample was then collected from the feed. The flow rate was subsequently reduced to 10 rpm, and a +1.0 V potential was applied to the cell for 10 min to facilitate the charging/adsorption process. After this charging phase, the circulating solution was gathered for further analysis. Then, 50 ml of DI water was introduced into the cell at no applied voltage to flush out residual ions from the electrode, a step repeated until the conductivity stabilized. For Li-ion desorption from the electrodes, 50 ml of fresh DI water was circulated for 15 min at a reverse potential of -1.0 V. A second desorption step involved a -1.2 V potential with a new 50 ml DI water batch to ensure complete ion release. Conductivity and pH were monitored throughout the charging and discharging phases using a conductivity meter. This sequence constituted one complete cycle, and the process was repeated five times (5 cycles) for each type of electrode.

Samples for Li concentration analysis were collected before and after charging, and following each desorption stage. These samples were analyzed using an inductively coupled plasma (ICP)-optical emission spectrometer (OES) instrument (ICP5000 Dual View, PG Instruments, Lutterworth, UK), calibrated with standard Li solution.

2.5.3. Evaluation methods

To evaluate the adsorption/desorption performance of both commercial and fabricated electrodes, the salt adsorption amount (Γ) was first calculated using:

$$\Gamma = V_f \int_0^t (C_0 - C_f) dt \quad (2)$$

Here, Γ represents the salt adsorption amount (μmole), V_f is the flowing solution volume (L), t is the duration (s), and C_0 and C_f (mM) are the ion concentrations in the solution before and after MCDI adsorption, respectively.

Expressed in relation to the mass of the working electrode (m), Γ is given by:

$$\Gamma_{Li} = \frac{(C_0 - C_f)}{m} V_f \quad (3)$$

To determine the amount of Li^+ recovered from the source solution per electrode mass unit, multiply Γ by the salt's molecular weight and divide by the cathode mass. This value, presented in Eq. (4), is termed as the salt adsorption capacity (SAC) or recovery capacity (RC) in mg/g.

$$\text{SAC} = \frac{\Gamma \times MW}{m \times 1000} \quad (4)$$

The salt adsorption rate (SAR) or recovery rate (RR) can then be derived as:

$$\text{SAR} = \frac{\Gamma}{t_{\text{charge}}} \quad (\mu\text{mole/s}) = \frac{\text{SAC}}{t_{\text{charge}}} \quad (\text{mg} \cdot \text{g}^{-1} \cdot \text{s}^{-1}) \quad (5)$$

To determine the charge efficiency (Λ) of the tested electrodes, the salt adsorption amount is divided by the charge stored in the Electrode (Σ). The stored charge (Q) can be deduced from the integration of the current (I) over the charging time, as shown in Eq. (6), followed by converting it from Colomb (C) to moles using Faraday's constant ($F = 96,485\text{C/mol}$).

$$Q = \int_{t_0}^{t_f} I dt \quad (6)$$

$$\Lambda = \frac{\Gamma}{\Sigma} = \frac{(C_0 - C_f) \times V_f \times F}{Q \times MW} \quad (7)$$

The Li^+ removal efficiency was calculated using Eq. (8) as follows:

$$\eta_M(\%) = \frac{C_0 - C_t}{C_0} \times 100 \quad (8)$$

For assessing the selectivity of the fabricated electrodes toward Li^+ , the separation factor ($\alpha_{M^{n+}}^{\text{Li}^+}$) was used. It connects the electrode's adsorption preference for Li^+ to its preference for another cation M^{n+} (e.g., Na^+ , K^+ , Ca^{2+} , and Mg^{2+}). The metric was derived from:

$$\alpha_{M^{n+}}^{\text{Li}^+} = \frac{\text{Adsorption ratio}_{\text{Li}}}{\text{Adsorption ratio}_M} \quad (9)$$

$$\text{Adsorption ratio} (M^{n+}) = \frac{C_0 - C_t}{C_0} \quad (10)$$

Lastly, the specific energy consumption was evaluated using:

$$E_{\text{SEC}} = \frac{E_{\text{ads}} \int_{t_0}^{t_f} I_{\text{ads}}(t) dt + E_{\text{des}} \int_{t_0}^{t_f} I_{\text{des}}(t) dt}{V} \quad (11)$$

Where E , I , and t represent voltage, current, and time, respectively. The subscripts 'ads' and 'des' signify the adsorption and desorption stages, respectively. Additionally, V denotes the volume of water treated in one cycle.

3. Results and discussion

3.1. Characterization of active material

Fig. 3a and c present the XRD diffraction patterns for the fabricated Li-deficient LiMn_2O_4 and LiAlO_2 (LMO and LAO) active materials. These patterns, plotting diffraction angles (2θ) against their intensities, show sharp peaks for both materials, indicating their high purity and crystallinity. Fig. 3a shows the XRD patterns of the LMO sample, with distinct peaks at angles 18.67° , 36.19° , 44.00° , 58.24° , 63.98° , and 68.37° , corresponding to the (111), (311), (400), (511), (440), and (442) crystal planes of spinel LMO. These findings are consistent with previous literature and match the standard cubic spinel phase of LMO in the Fd-3 m space group (ICDD:98-009-4339) [28,34,35], confirming the material's structure. Fig. 3b illustrates the spinel structure of LMO, where manganese ions occupy octahedral sites surrounded by oxygen ions, and vacancies enhance Li ion diffusion [19]. Li and Mn are positioned in tetrahedral (8a) and octahedral (16d) sites, respectively, within a cubic oxygen framework.

Fig. 3c presents the XRD spectra for LAO, showing peaks for the miller indices (003), (101), (012), (104), (015), (009), (107), (018), and (110) at 2θ angles of 18.71° , 37.59° , 39.22° , 45.48° , 49.35° , 58.37° , 59.30° , 65.02° , and 66.76° . These peaks indicate the presence of primarily α - LiAlO_2 phase, along with signs of γ - LiAlO_2 , suggesting a mixture of these phases. Notably, α - LiAlO_2 exhibits a hexagonal crystal system within the R-3 m space group (ICDD:98-002-8288), while γ - LiAlO_2 is characterized by a tetragonal crystal system in the P 41 21 2 space group (ICDD:98-003-0249) [27,36], as detailed in Fig. 3d.

XPS analysis was employed to analyze the chemical and elemental compositions, including oxidation states, of LiMn_2O_4 and LiAlO_2

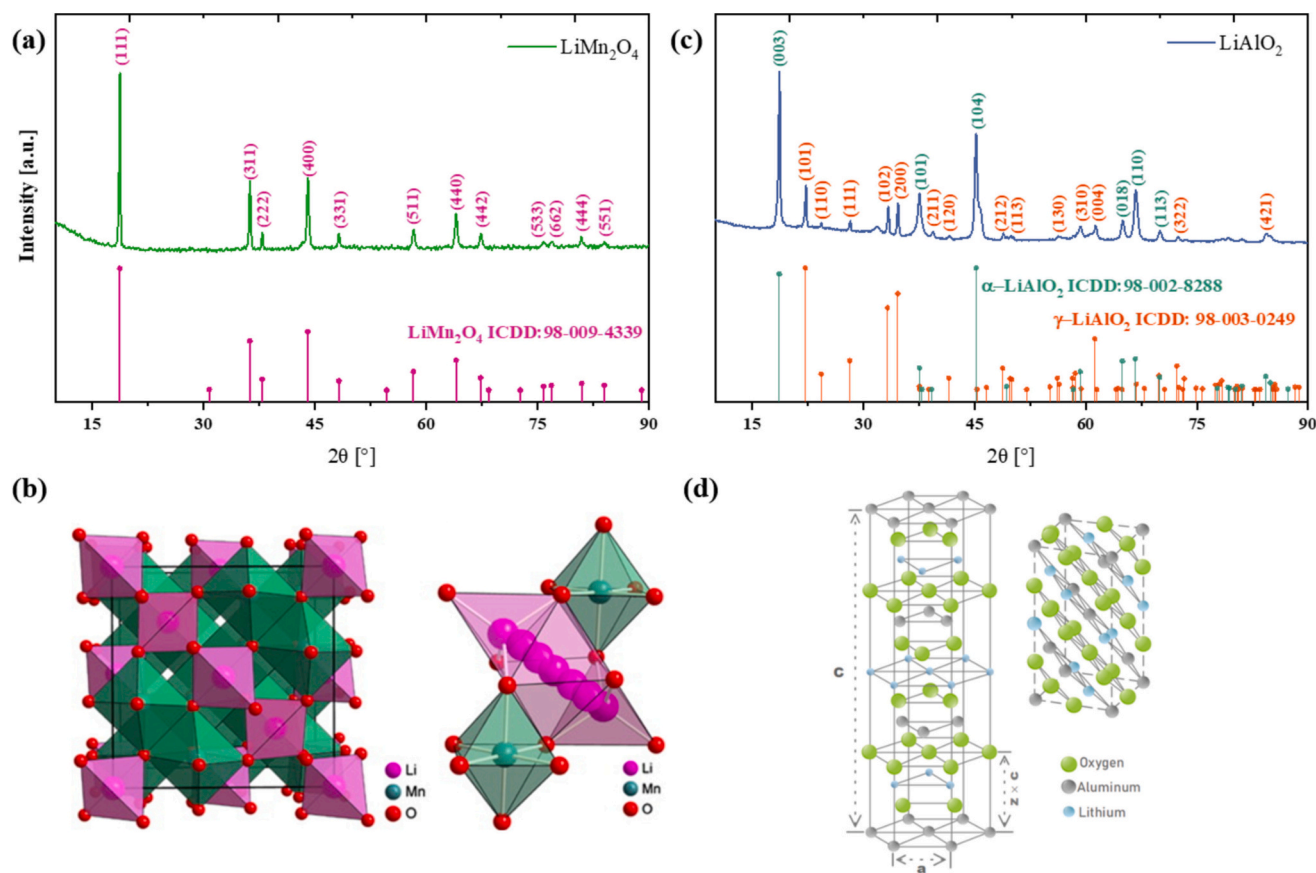


Fig. 3. X-ray diffraction (XRD) patterns and crystallographic structures: XRD patterns of prepared LiMn_2O_4 and LiAlO_2 materials (a, c) and crystallographic structures of spinel LiMn_2O_4 and LiAlO_2 (b, d) [36,37].

materials, as shown in Figs. 4a–c and 5a–c. The survey spectrum (Fig. 4a) ranged from -10 V to 1350 V, using a 1 eV step size and a 100 -eV pass energy, confirming the presence of carbon (C), manganese (Mn), and oxygen (O) in line with previous studies [28,34]. The wide-scan XPS spectra displayed peaks for Mn 2p, O 1s, and C 1s at binding energies of 642.77 , 530.9 , and 284.86 eV, respectively, with atomic ratios of 22.67% for Mn 2p, 58.98% for O 1s, and 18.36% for C 1s. High-resolution core-level XPS spectra were taken with a 20 eV pass energy and a 0.1 V step size, detailed in Fig. 4b and c. In Fig. 4b, the Mn 2p spectrum showed two main peaks at 654 and 642.4 eV, indicating Mn $2p_{1/2}$ and Mn $2p_{3/2}$ spin-orbit coupling states and a Mn oxidation state of $2+$ [38]. The spin energy difference of 11.6 eV matches the characteristics of MnO_2 [39]. Peaks at 641.7 eV and 643.5 eV represent Mn^{3+} and Mn^{4+} states, respectively. The O 1s spectrum in Fig. 4c is deconvoluted into peaks at 529.5 , 530.9 , and 533.2 eV, correlating with Mn-O, Mn-OH, and C-O bonds [34]. The absence of a significant Li 1s signal suggests a low Li surface concentration, confirming the intended Li-deficient state of the LiMn_2O_4 electrode.

Fig. 5 illustrates the XPS spectra for the fabricated LiAlO_2 . The O 1s emission shows a notable peak at 531.26 eV, accounting for 60.91% of the atomic ratio, and the Al 2p peak at approximately 73.7 eV represents 22.04 atomic %. The spectrum also identifies a Li 1s presence at 54.69 eV. The C 1s peak, located around 284.67 eV, serves as a calibration reference [40]. Fig. 5b and c reveal convolutions in Al 2p and O 1s spectra, with O 1s peaks at 531.0 and 532.4 eV corresponding to Al-O-Al and Al-OH bonds within the LiAlO_2 structure [41,42]. The primary peak for Al at 73.7 eV, below 74.3 eV typically seen for Al_2O_3 , verifies the presence of LiAlO_2 in the sample [43].

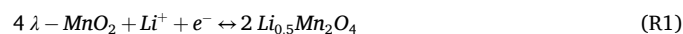
To characterize the morphological structure of the synthesized materials, SEM and TEM analyses were performed, complemented by EDS for elemental mapping, as presented in Figs. 4d–i and 5d–i. The SEM and

TEM images (Fig. 4d and e) depict particles with a consistent rod-like shape, measuring approximately $2 \mu\text{m}$ in length and 500 nm in width, consistent with those typically formed through solid-state reaction synthesis of LiMn_2O_4 [44]. The elemental mapping displayed in Fig. 4f–i shows a uniform distribution of manganese (shown in purple) and oxygen (in red) across the examined sample, with mass percentages of around 57.2% and 34.9% , respectively. Trace amounts such as C, Mg, Al, and Cl were also detected.

For the LiAlO_2 material, depicted in Fig. 5, the morphology consists of irregularly shaped, agglomerated particles, a common characteristic of such materials as supported by previous studies [42,45]. TEM analysis (Fig. 5d) reveals these agglomerates as single units, roughly $1 \mu\text{m}$ in size. EDS mapping in Fig. 5f–i further confirms an even distribution of Al and O throughout the sample, verifying the successful fabrication of the LiAlO_2 material.

3.2. Electrochemical characterization of MCDI electrodes

The electrochemical properties of the fabricated LMO and LAO electrodes were initially assessed using CV tests. Fig. 6a and b present the CV profiles of LMO and LAO electrodes in 1 M LiCl and NaCl solutions within a potential range of 0 to 1.1 V. The CV curve of the pure LMO-based electrode, shown in Fig. 6a, obtained at a scan rate of 1 mV/s, reveals two distinct reversible redox peaks at $0.76/0.60$ and $1.0/0.90$ V, consistent with previous findings [46,47]. These peaks reflect the two-step reversible intercalation/de-intercalation processes of Li^+ ions within the spinel LMO structure at specific lattice sites [47], represented by the reactions:



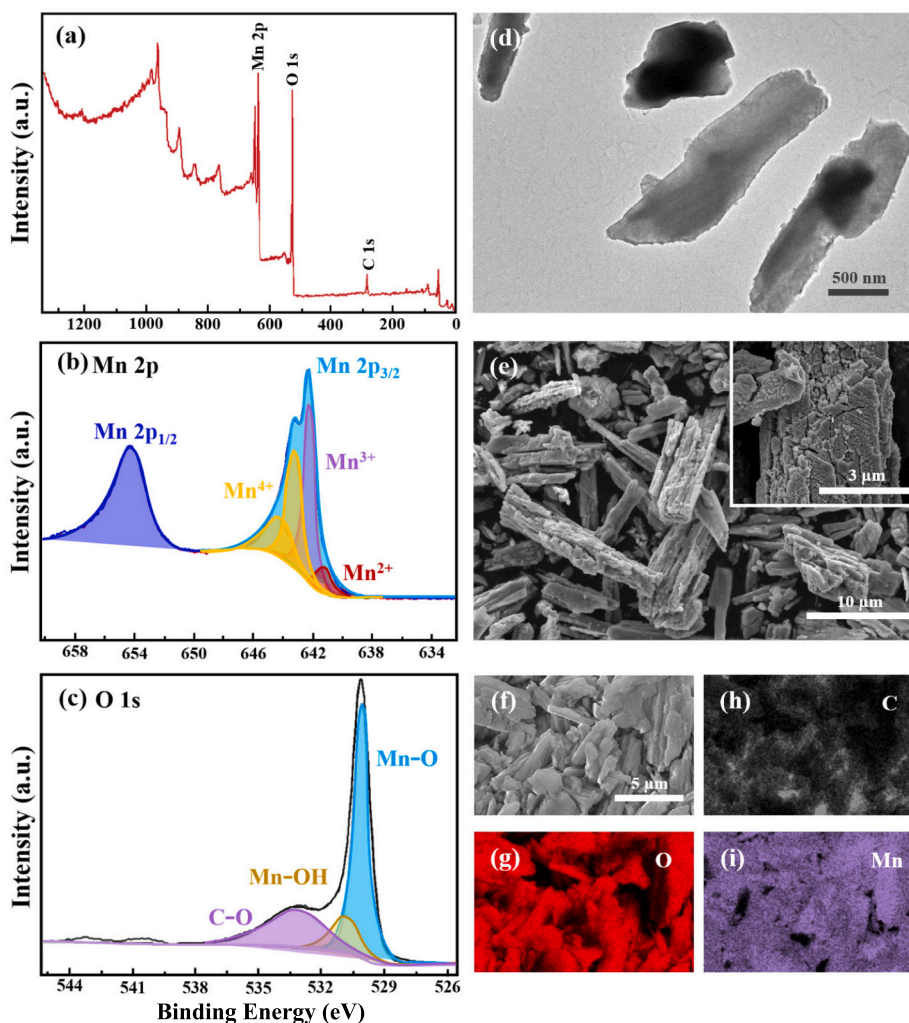
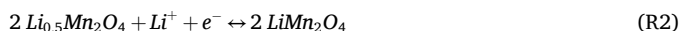


Fig. 4. XPS and morphological analyses of fabricated LiMn_2O_4 : (a) a wide survey XPS spectrum, (b) high-resolution Mn 2p spectra, and (c) O 1s spectra. Morphological characterization of LiMn_2O_4 : (d) TEM image, (e) SEM images, and (f–i) EDS elemental mapping.



At 0.76 V, the charging process involves Li^+ ions migrating from the electrolyte to the λ - MnO_2 cathode and inserting into half of the tetrahedral sites marked by Li–Li interactions, leading to the formation of $\text{Li}_{0.5}\text{Mn}_2\text{O}_4$ Eq. (R1). This is accompanied by a reduction of Mn from Mn^{4+} to Mn^{3+} and an expansion of the crystal structure. At 0.6 V, the additional Li ions intercalate, transforming the material to LiMn_2O_4 and completing the lithiation process Eq. (R2). The discharge peaks at 0.90 and 1.0 V reflect the de-intercalation of Li ions [48], leading the material back to its original λ - MnO_2 configuration with the oxidation of Mn^{3+} to Mn^{4+} [37].

Fig. 6b shows the CV curve of LAO with prominent redox peak pairs at 0.90/0.70 and 0.8/0.75 V, indicative of the typical two-step Li insertion and extraction in the de-lithiated LAO structure (Eq. (R3)) [36].



Both electrode types exhibited enhanced capacitance in 1 M LiCl compared to 1 M NaCl, suggesting superior Li^+ ion conductivity and affinity in the cathode materials over Na^+ ions.

Fig. 6c shows the CV curves for both the pure and mixed LMO and LAO electrodes along with the commercial activated carbon (AC) electrode. The electrodes with varying ratios (%) of LMO to LAO (90/10, 80/20, 50/50, 20/80, 10/90) exhibit different capacitive behaviors and

varying prominence of faradaic reaction. The pure LMO electrode displays the largest area under the curve, indicating the highest capacitance, while the pure LAO electrode has the smallest. As for peak definition, the pure LAO electrode exhibits sharper oxidation and reduction peaks, demonstrating efficient Faradaic reactions and facilitated Li^+ intercalation/de-intercalation. Transitioning from pure LMO to higher LAO content, there is a noticeable decrease in oxidation potentials and an increase in reduction potentials, suggesting reduced electrochemical polarization and improved redox reversibility.

To further assess and quantify the charge/discharge behavior of the fabricated electrodes, GCD analysis was conducted using a 1 M LiCl electrolyte solution, as depicted in Fig. 6d. The GCD profiles are arranged to provide a seamless transition from the charging to the discharging phase, with each charging curve terminating at its plateau, followed immediately by the corresponding discharge curve. From these profiles, the specific capacitance values were calculated for each electrode using Eq. (1), as shown in Fig. 6e. During the charging phase, both the single LMO and the LMO/LAO (90/10) blend showed gradually increasing charging curves, reaching higher potential differences of 1.79 V and 1.69 V, respectively. These values indicate superior performance and increased capacitance compared to other electrodes, which achieved their peak charging potentials more quickly, suggesting lower intercalation capacities. In contrast, the AC electrode demonstrated the smallest potential difference (1.4 V), highlighting the significant impact of the Li^+ intercalation mechanism on effective charge storage and

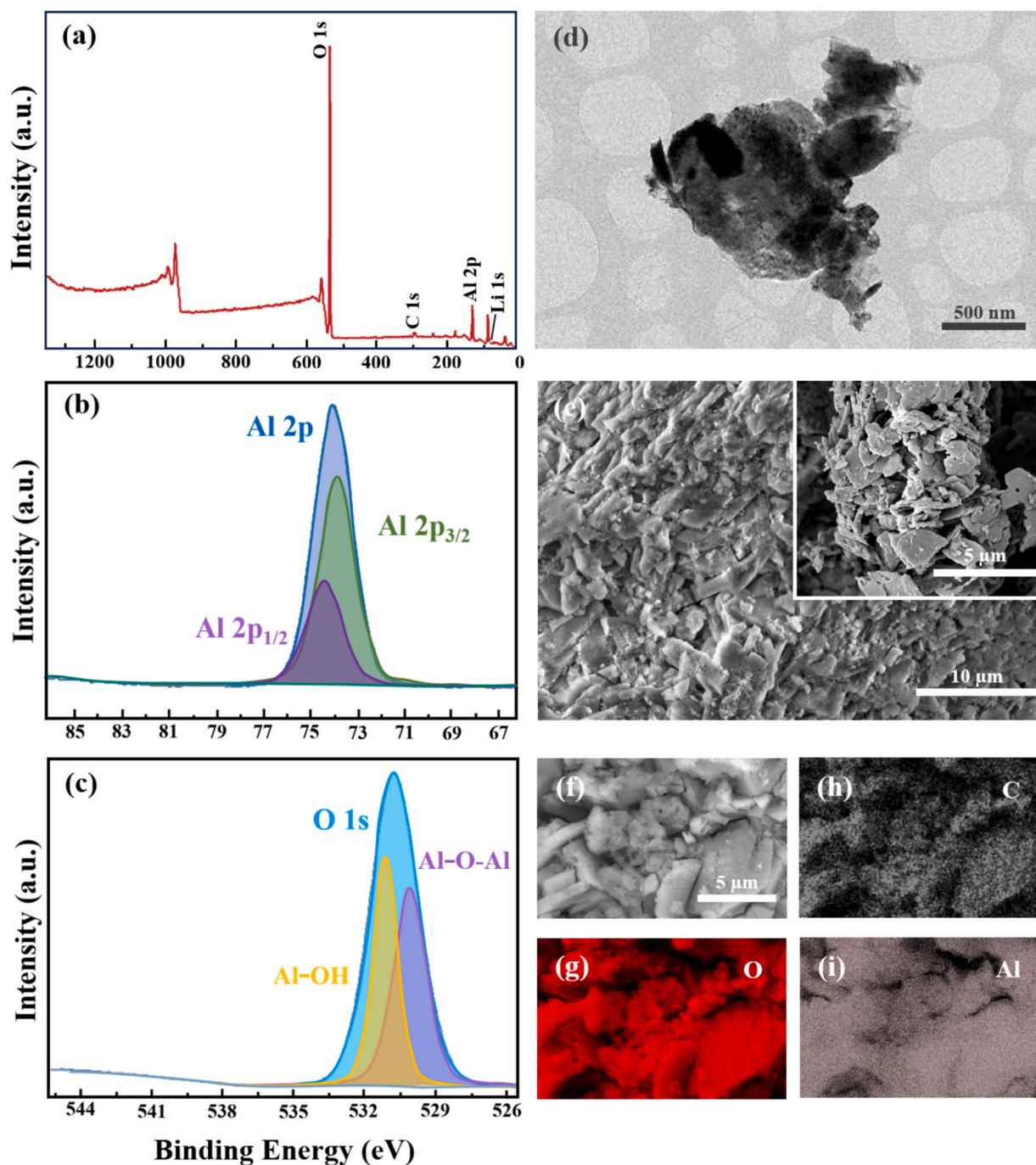


Fig. 5. XPS and morphological analyses of fabricated LiAlO_2 : (a) a wide survey XPS spectrum, (b) high-resolution Al 2p spectra, and (c) O 1s spectra. Morphological characterization of LiAlO_2 : (d) TEM image, (e) SEM images, and (f–i) EDS elemental mapping.

cation retention, as opposed to the non-Faradaic process of surface ion adsorption.

Analysis of the GCD profiles and the calculated capacitance values reveals that the LMO electrode demonstrated the slowest charging rate but reached the highest peak potential. Conversely, its discharge curve was notably short, indicating a high discharge rate, with all intercalated ions released in around 170 s, resulting in a specific discharge capacitance of about 96.15 F/g. Adding 10 % by weight of LAO enhances discharge performance, as seen in the LMO/LAO (90/10) electrode, which showed the longest discharge duration of 290 s, reflecting a higher specific capacitance of 159.6 F/g than other tested electrodes. However, increasing the proportion of LAO leads to a gradual decrease in specific capacitance.

EIS was utilized to assess changes in impedance at the cathode-electrolyte interface and to investigate the kinetics of Li^+ diffusion within the cathode. Nyquist plots for most electrodes displayed distinct curves with notably low resistance values across the frequency range. These plots typically exhibit a semicircular pattern at higher frequencies and a linear pattern at lower frequencies. An equivalent circuit, which included constant phase elements (CPE_1 and CPE_2) and finite Warburg impedance, was used for analysis. As illustrated in Fig. 6f, this circuit model helped distinguish different components of the Nyquist plot: an ohmic resistance (R_s) at high frequencies, two semicircles at high-to-medium frequencies representing film resistance (R_{sf}) and charge transfer resistance (R_{ct}), and a sloped line at lower frequencies that suggests Li^+ diffusion within the electrode material [34]. The size of the

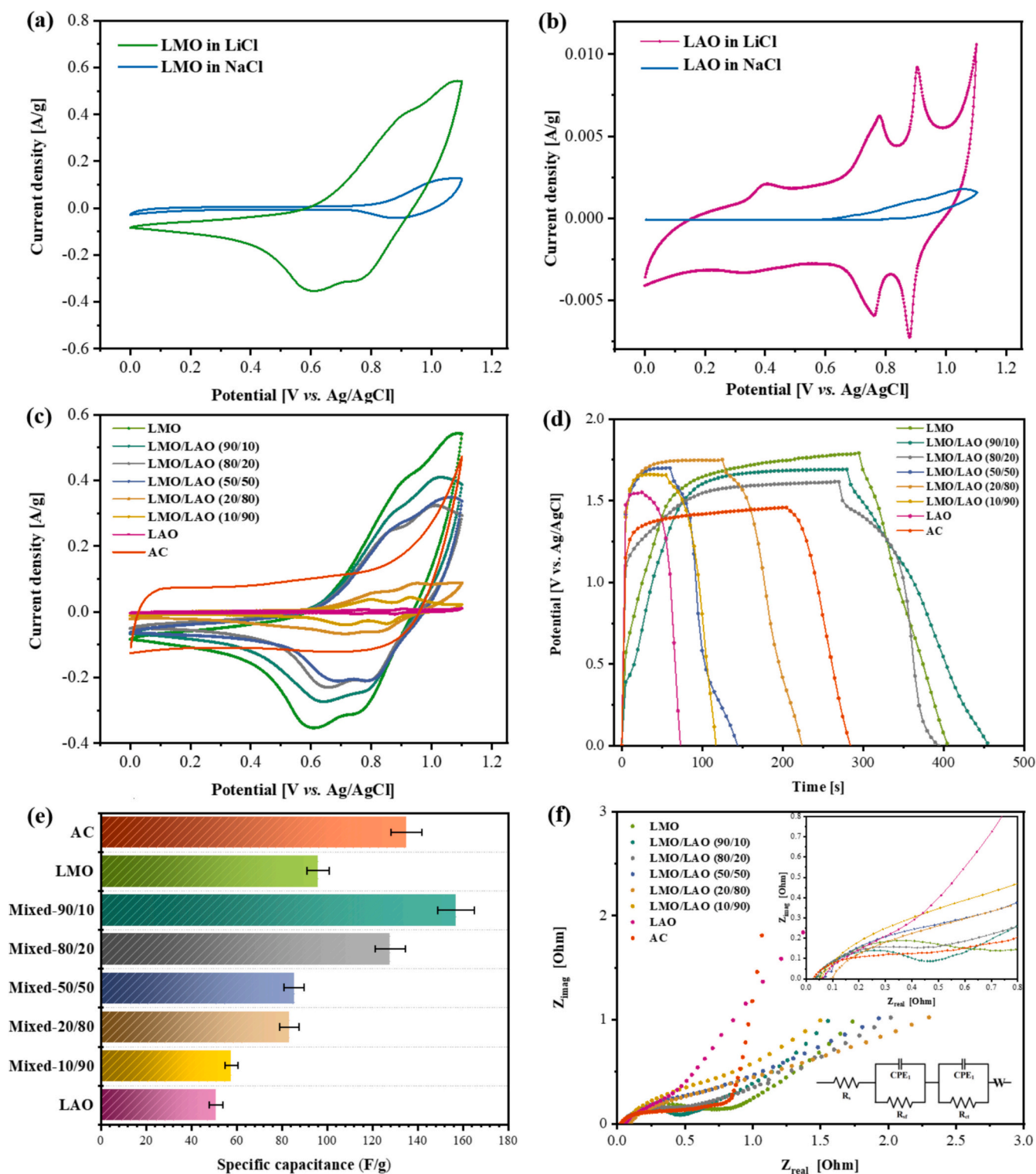


Fig. 6. Electrochemical characterization of fabricated electrodes: Cyclic voltammetry (CV) curves for (a) LMO and (b) LAO in 1 M NaCl and LiCl solutions, scan rate of 1 mV/s. (c) CV performance comparison of all tested electrodes in 1 M LiCl solution at a scan rate of 1 mV/s. (d) Charge-discharge time profiles for various tested electrodes at a current of 0.15 A. (e) Specific capacitance correlated with the charge-discharge profiles. (f) Electrochemical impedance spectroscopy (EIS) plots and equivalent circuits for the fabricated electrodes and AC electrodes within the frequency range of 0.01 Hz to 100 Hz.

semicircle directly reflected the R_{ct} .

The EIS profiles revealed a short circuit pattern with a low R_{ct} for the pure LMO electrode, while the pure LAO electrode exhibited a more open circuit pattern. Electrodes with mixed components showed R_{ct} values between these two, with the LMO/LAO (90/10) electrode displaying the lowest R_{ct} , approximately 0.2 Ω , suggesting efficient charge

transfer and enhanced electrochemical performance [35]. A higher concentration of LAO corresponded with an increase in R_{ct} . In contrast, the Nyquist plot for the commercial AC electrode predominantly featured a finite space Warburg impedance pattern, which differed from the semi-infinite Warburg impedance observed in other electrodes.

The electrochemical performance profiles emphasize the advantage

of blending a suitable amount of LAO with LMO to enhance specific discharge capacitance. Prior research on integrating LAO into Li-ion battery electrodes reveals potential mechanisms behind this performance enhancement. According to Gao, Jian, et al. [49], the ionic conductivity of bulk LAO at room temperature is approximately 10^{-21} S cm^{-1} , which is a notably low value and would ideally hinder ion transfer within the material. However, the application of a voltage bias in the electrochemical CDI system significantly increases this conductivity by enhancing both external Li sources (like interstitials/vacancies reservoirs) and charge carriers (electrons/holes) [43].

Additionally, the strategic incorporation of LAO to form a composite with LMO enhances the Li-ion conductivity of the resulting material. This improvement is primarily due to the growth of the LAO phase over grain boundaries, which facilitates the movement of Li ions within these regions, thus reducing grain boundary resistance [50]. Additional studies, such as those by Pritee Wakudkar et al. [51], corroborate these findings. They attributed the increased conductivity to a Li-conducting phase at the grain boundaries, consisting of LiO_4 and AlO_4 tetrahedra where Li and Al atoms occupy oxygen tetrahedral sites. These tetrahedra share corners, forming conductivity channels to Li-ion diffusion along the (100) and (001) directions. LAO's ionic conductivity is associated with structural disorder from point defects, as supported by density functional theory (DFT), where Li ion migration occurs through Li point defects and Frenkel defects between tetrahedra. The presence of Li vacancies and interstitial Li strongly influences Li conductivity [52]. Furthermore, Al incorporation from LAO into the lattice suggests that Al^{3+} can substitute for 3 Li^+ to maintain charge neutrality. This substitution leads to the creation of two additional vacancies, thereby increasing the Li vacancy concentration and, consequently, the overall conductivity of the material [51].

Overall, LAO acts as a conductive network within the LMO/LAO

composite, facilitating Li-ion hopping and enhancing the kinetics of Li^+ intercalation and de-intercalation in LMO. This results in improved specific capacitance and electrochemical performance. Analysis of the GCD profile reveals that incorporating 10 % LAO with LMO yields the best performance, marking the optimal composition for the electrode's peak efficiency. Increasing the LAO content beyond this percentage leads to a noticeable reduction in performance due to the inherently poor conductivity of bulk alumina. Excessive LAO can obscure the active sites in LMO, hindering the flow of Li ions and thereby reducing the electrode's overall electrochemical efficiency [27,40].

To further understand the impact of morphological characteristics on the performance of the LMO/LAO (90/10) electrode, high-resolution SEM imaging, and EDS mapping were employed, with results presented in Fig. 7. Fig. 7a displays the micrographs of the LMO/LAO (90/10) mixed electrode, showing a densely packed pallet morphology with an organized structure. Compared to the pure LMO electrode (Fig. 7b), which features loosely connected granules, the addition of LAO results in a denser microstructure with granules in close contact and minimal voids, facilitating efficient electron migration. This denser structure is due to the growth of the LAO phase at the grain boundaries. EDS mapping for Al and Mn (Fig. 7c–g) identifies distinct areas with small patches of Al embedded among the predominant Mn atoms, which act as a binder enhancing Li^+ ion migration within the composite, effectively securing them in the material. This morphology aligns with similar findings reported earlier [51]. The incorporation of LAO alters the microstructure and serves as a key factor in promoting Li-ion conductivity within the composite. In each evaluated electrode, the close interaction between the active materials and amorphous carbon forms a robust conductive network, facilitating the transfer of both Li-ions and electrons [41].

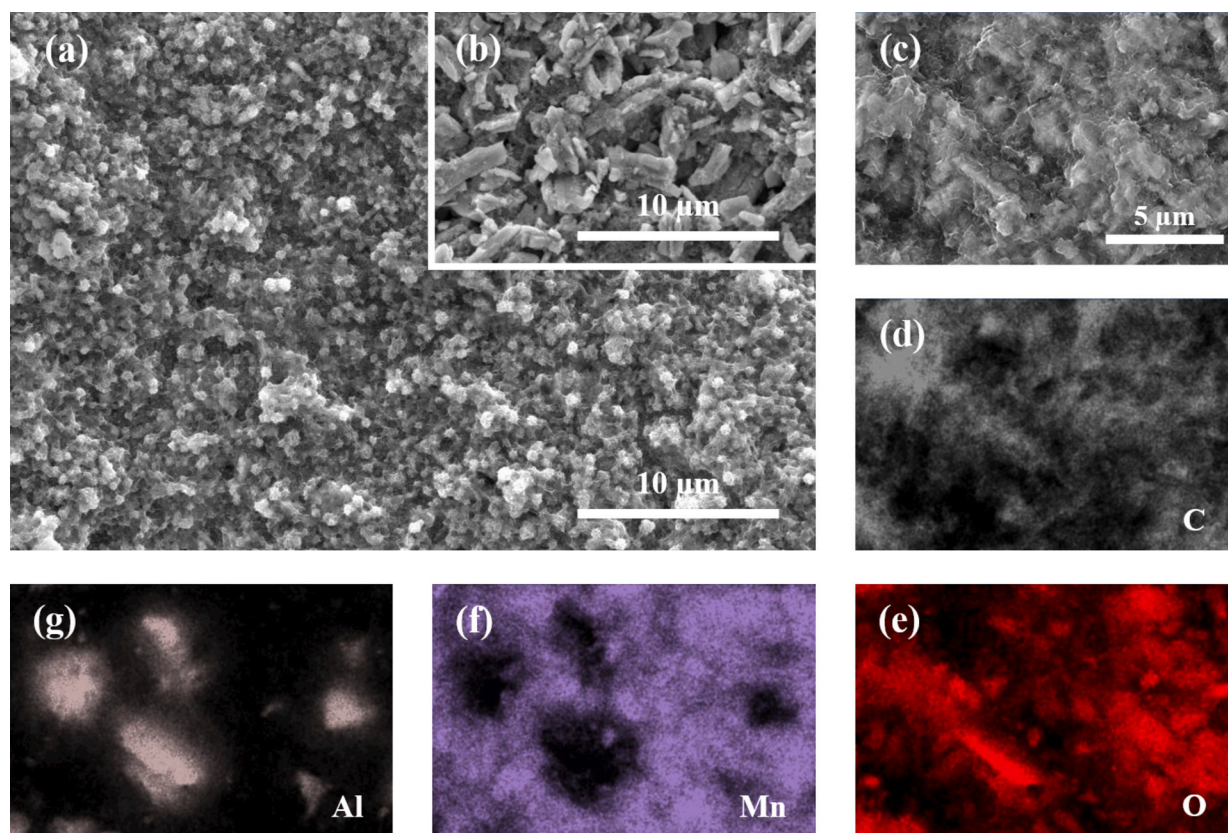


Fig. 7. Microscopic and elemental analysis of electrodes: (a) SEM images of LMO/LAO (90/10)-CDI electrode at magnifications(10,000 ×). (b) SEM image of LMO-CDI electrode. (c) SEM images of LMO/LAO (90/10)-CDI electrode at magnifications (15,000 ×). (d–g) EDS elemental mapping for C, O, Mn, and Al in the LMO/LAO (90/10)-CDI electrode.

3.3. Test of electrodes in MCDI for Li^+ recovery

3.3.1. Charge/discharge performance of activated carbon and LMO electrodes

To evaluate the Li^+ capture performance in the MCDI cell, the tested electrodes functioned as the cathode (negative electrode), with a commercial activated carbon (AC) electrode used as the anode (positive electrode). Fig. 8a–c presents the MCDI performance utilizing AC electrodes as both roles, illustrating (a) the current profile (in Amperes, A), (b) the accumulated charge on the electrode (in micromoles per grams of active material, $\mu\text{mol/g}$), and (c) the change in concentration profile (mM) of LiCl over three charge/discharge cycles, where $\Delta C = C_f - C_0$. Each cycle includes four phases, starting with introducing a 5 mM LiCl solution into the cell for 10 min at a cell potential of 1.0 V during Phase 1 (Charging). In this phase, both cations (Li^+) and anions (Cl^-) are adsorbed into the micropores of the AC electrodes. The resulting chronoamperograms (Fig. 8a) show a rapid current surge, peaking at an average of 0.039 A, followed by a gradual exponential decrease to near zero, a pattern consistent with previous constant voltage CDI studies [53,54]. The electrodes accumulated about 95.12 $\mu\text{mol/g}$ of charge, corresponding to a decrease in the effluent LiCl concentration by a ΔC of 0.43 mM, achieving a maximum Li adsorption capacity (SAC) of 4 mg/g during the initial cycle, which diminished in subsequent cycles.

Following this, DI water was introduced to rinse any non-adsorbed Li ions until the effluent solution's conductivity stabilized (Phase 2: Rinsing). Phase 3 (Discharging) involved introducing fresh DIW with a -1.0 V reverse cell potential, facilitating the release of adsorbed Li ions

into the flow. A second discharge (Phase 4) employed a -1.2 V potential to ensure all Li ions were released from the electrode voids, preparing the system for subsequent cycles. During these discharging phases, the accumulated charge showed a sharp initial decrease followed by an exponential rise until stabilization. The initial significant drop in the current discharge profile indicates rapid desorption of a large fraction of adsorbed ions, driven by the electric field, transitioning to a gradual increase as ion desorption becomes diffusion limited. As the system approaches saturation, the ion release stabilizes, and the profile levels off [16].

Subsequent investigations focused on the performance of the pure LMO-CDI electrode to assess the impact of utilizing Li-specific intercalating material within the MCDI Li capturing system, with findings presented in Fig. 8d–f (green-colored profiles). The LMO-CDI electrode functioned as the negative cathode against a positive AC electrode in this configuration. As shown in Fig. 8d, the current profile resembles that of the AC-AC MCDI experiment, peaking at 0.03 A and then dropping to -0.005 A during the second cycle. In Fig. 8e, the charge profiles reach up to 137.5 $\mu\text{mol/g}$, significantly higher than the 96.1 $\mu\text{mol/g}$ observed for the AC electrode, and exhibit sharper rises and falls, suggesting a greater ion adsorption and intercalation capacity within the LMO electrode's lattice. Fig. 8f shows a rapid decrease in the effluent solution's concentration during the initial minutes of charging, with a notable drop of 1.89 mM in the second cycle. During the discharge step, the concentration stabilizes within 15 min, indicating a recovery of around 72.5 % of the previously adsorbed/intercalated ions back into the water flow. The electrode underwent five cycles to verify the consistency of the

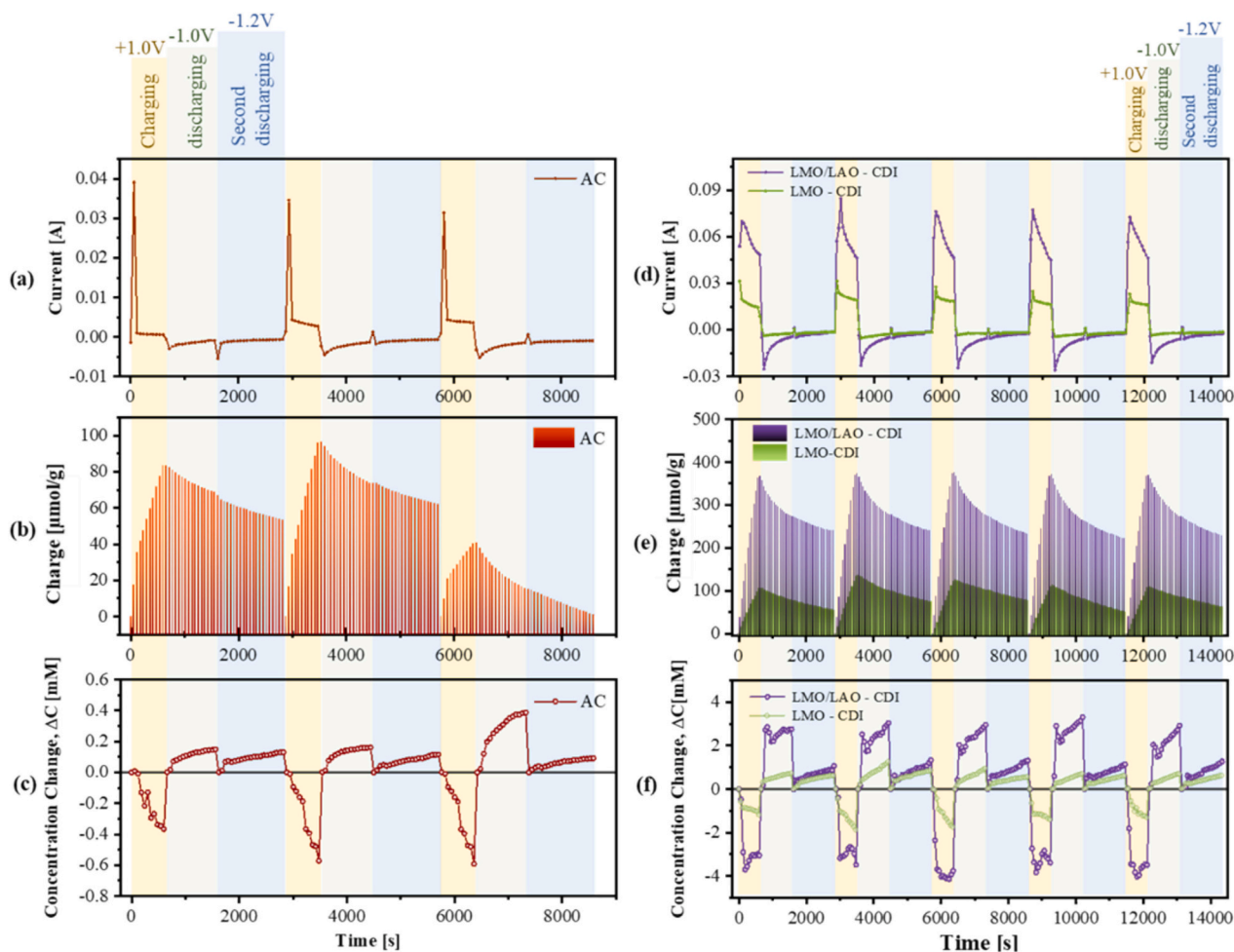


Fig. 8. Charge/discharge performance of electrodes in the MCDI Li capturing system using a 5 mM LiCl feed solution across 3–5 cycles: (a, d) Current profiles for AC-CDI (red), LMO-CDI (green), and LMO/LAO-CDI (purple) electrode. (b, e) Profiles of accumulated charge on each electrode. (c, f) Concentration change profiles.

charge/discharge process and the durability of the Li intercalating material. Notably, with successive cycles, the amount of extracted Li increased, contrasting with the declining current trend observed in Fig. 8a. Fig. 9 illustrates the detailed mechanism of the Li^+ intercalation process within the MCDI system across four repeated steps.

3.3.2. Performance of LMO/LAO mixed electrode for Li^+ recovery

The electrochemical analysis indicates that the LMO/LAO (90/10) electrode outperformed others, displaying the highest specific capacitance and the lowest charge transfer resistance. Thus, it was chosen for the MCDI Li^+ recovery test to assess its performance and Li selectivity within the MCDI cell. Fig. 8d–f presents the test results for the LMO/LAO (90/10) electrode, comparing these with the pure LMO electrode under

the same conditions. Notably, the mixed electrode significantly improves both current and accumulated charge compared to the pure LMO electrode. This increased charge correlates with a rapid decline in the LiCl effluent concentration during the first 3 min of charging, decreasing from 5 mM to an average of 2 mM and then moderately rising to stabilize at around 3 mM by the end of the charge phase. Fig. 10a depicts a detailed view of this ΔC -time profile, specifically highlighting the second cycle. It illustrates a more pronounced reduction during the charging step for the LMO/LAO (90/10) electrode compared to the pure LMO and AC electrodes, reaching the highest adsorption amount of 900 $\mu\text{mol/g}$ of active cathode material. In contrast, the LMO and AC electrodes exhibited slower Li adsorption rates of 365 $\mu\text{mol/g}$ and 57.7 $\mu\text{mol/g}$, respectively, as shown in Fig. 10b.

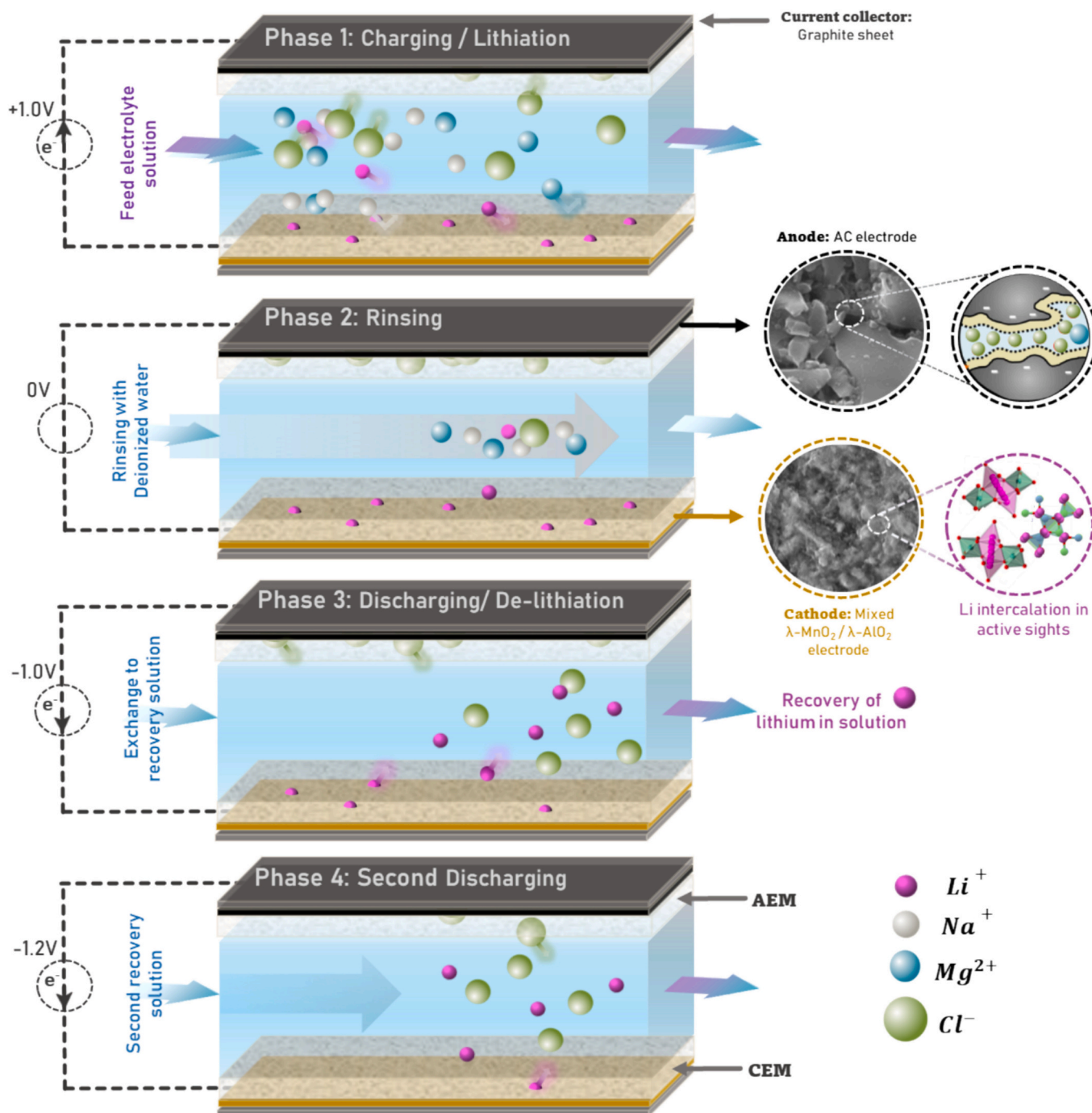


Fig. 9. Visualization of the Li^+ intercalation process in the MCDI system.

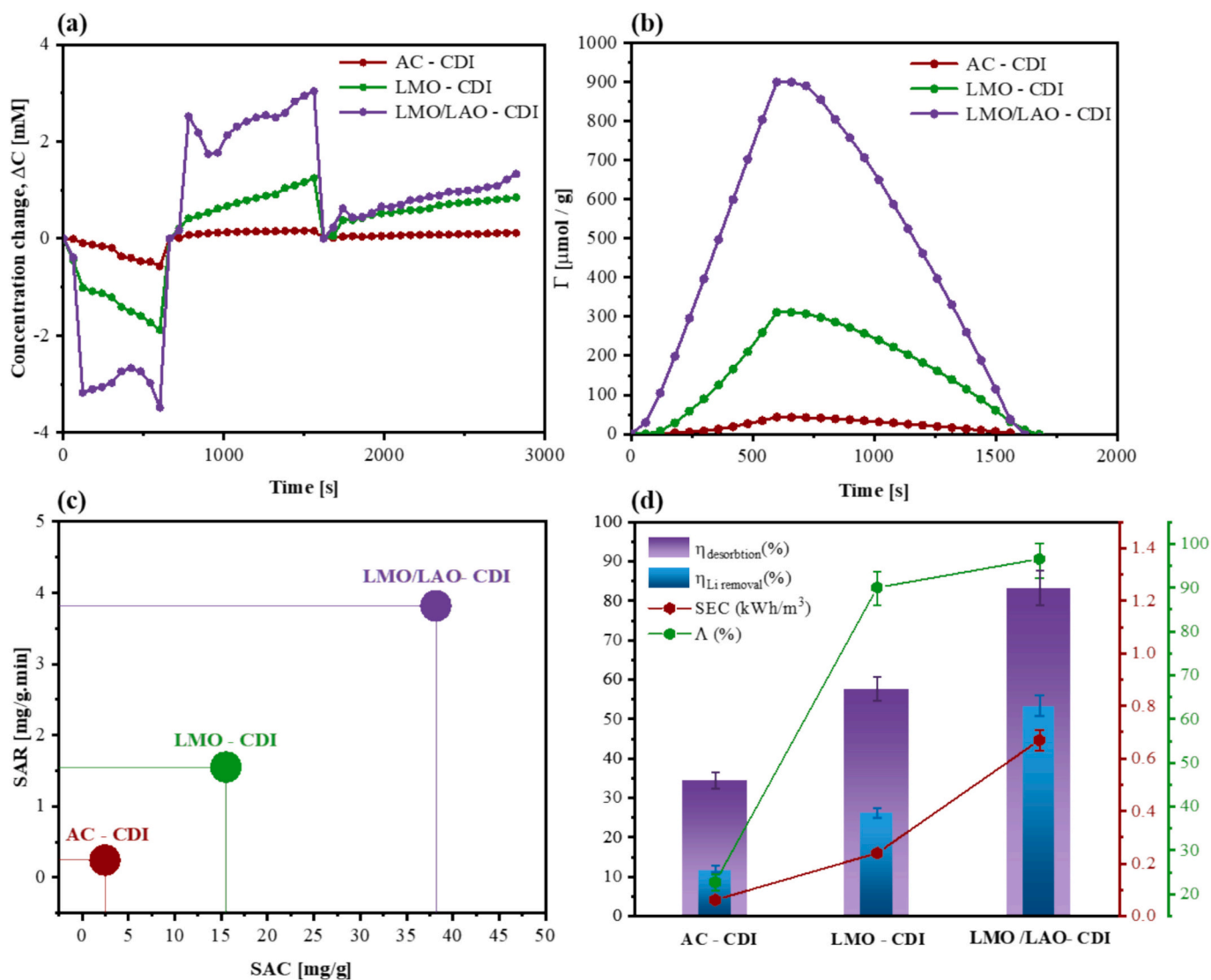


Fig. 10. Comparative performance of AC-CDI, LMO-CDI and LMO / LAO-CDI electrodes in MCDI Li capturing system with a 5 mM LiCl feed solution: (a) Change in concentration profile (ΔC). (b) Li adsorption amount (Γ) profile. (c) Li salt adsorption rate (SAR) and capacity (SAC). (d) Desorption efficiency ($\eta_{\text{desorbition}}$), Li removal efficiency ($\eta_{\text{Li removal}}$), the specific energy consumption (SEC) of the system, and charge efficiency (Λ).

Fig. 10c highlights the superior Li recovery performance of the mixed electrode by comparing the SAC and SAR of each tested electrode. The progression from AC to the pure LMO and then to the mixed electrode shows data points ascending and moving right, indicating enhanced Li^+ recovery rates and amounts. The improved charge/discharge dynamics are attributed to including LAO, which potentially introduces a porous or modified structure that enhances Li ion diffusion within the electrode, thereby accelerating intercalation and de-intercalation rates [53]. Additionally, the presence of aluminum oxide acts as a conductive additive, forming pathways for efficient electron transport and reducing internal resistance [55]. As a result, integrating 10 % LAO with 90 % LMO leads to a notable 146 % improvement in both SAC and SAR values compared to the pure LMO electrode.

Fig. 10d presents various performance metrics, including charge efficiency (Λ), desorption efficiency (%), and Li removal efficiency. The mixed electrode outperforms others with a charge efficiency of 96.5 %, a Li removal efficiency of 53.2 %, and a high discharge efficiency of around 83.1 %. Furthermore, Fig. 10d outlines the specific energy consumption of the MCDI process, calculated using Eq. (11). This metric covers the energy used during the adsorption and desorption steps, excluding feed pumping energy. Energy consumption varied from 0.062

kWh/m^3 for the AC electrode to 0.67 kWh/m^3 for the mixed electrode. Although the mixed electrode's energy use was slightly higher, it still falls within the typical range for MCDI systems, which is between 0.2 and 1.5 kWh/m^3 [56].

Fig. 11 compares the specific adsorption capacity (SAC) of the mixed LMO/LAO MCDI electrode for Li recovery against similar MCDI systems from previous research (cited in Table 1). This comparison highlights the enhanced SAC of the LMO/LAO electrode within the examined concentration range compared to earlier results.

3.3.3. Effect of solution concentration on Li^+ recovery

The initial concentration of ions fed into the MCDI cell is a critical factor in the charge-discharge process. To study this effect, a series of charge/discharge cycles were conducted on the mixed LMO/LAO electrode to investigate how varying initial LiCl concentrations affect Li^+ capture efficiency. Fig. 12 presents the results of these tests across LiCl concentrations of 1.25 mM to 20 mM. Fig. 12a displays the charge/discharge time profiles, showing relative concentration (C_R) and concentration change (ΔC) for each initial concentration. Fig. 12b presents the associated performance metrics, such as the amount of Li adsorption (Γ , $\mu\text{mol/g}$), charge efficiency (Λ , %), and Li removal efficiency (η_{Li}

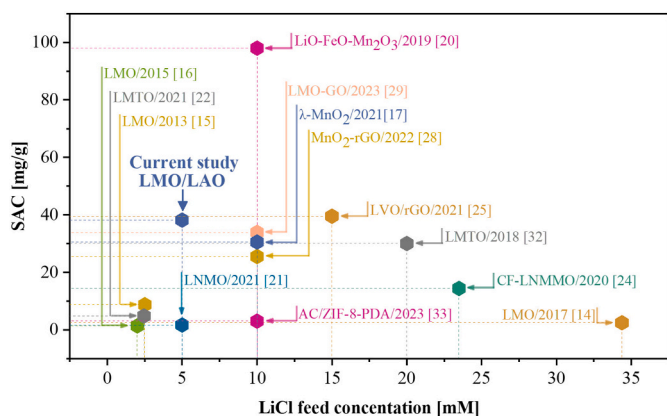


Fig. 11. Comparative analysis of salt adsorption capacity (SAC) between this study and previous research on MCDI Li⁺ capturing systems [14–17,20–22,24,25,28,29,32,33].

Removal, %).

During the charging phase, ΔC increases with raising initial concentration, correlating with a rise in Γ from 364.33 μmol/g at 1.25 mM to 976.47 μmol/g at 20 mM. This trend is attributed to enhanced

electrolyte conductivity at higher solution concentrations, facilitating charge and ion transfer within the MCDI system and expediting the reaction [20]. Lower initial concentrations show a gradual increase in effluent concentration as charging progresses, whereas higher concentrations, such as 10 mM and 20 mM, demonstrate an immediate surge in concentration difference followed by a leveling off at ΔC ~ 2.7 mM. This pattern suggests a saturation point in electroadsorption at these concentrations, beyond which no additional salt adsorption benefits from higher ion availability due to electrode intercalation sites saturation. This saturation point is already reached at 5 mM, where further concentration increases compress the electrical double layer (EDL) on the electrode surface, reducing charge storage capability and the amount of Li⁺ adsorbed per charging cycle, as indicated by reduced Li⁺ removal and charge efficiencies at higher salt concentrations (Fig. 12b).

In order to further study the electroadsorption properties of the fabricated and tested LMO/LAO electrodes, Langmuir (Eq. (12)) and Freundlich (Eq. (13)) adsorption isotherms were applied to the experimental data and the results are presented in Fig. 12c:

$$q_e = \frac{q_m K_L C_e}{1 + K_L C_e} \tag{12}$$

$$q_e = K_F C_e^{1/n} \tag{13}$$

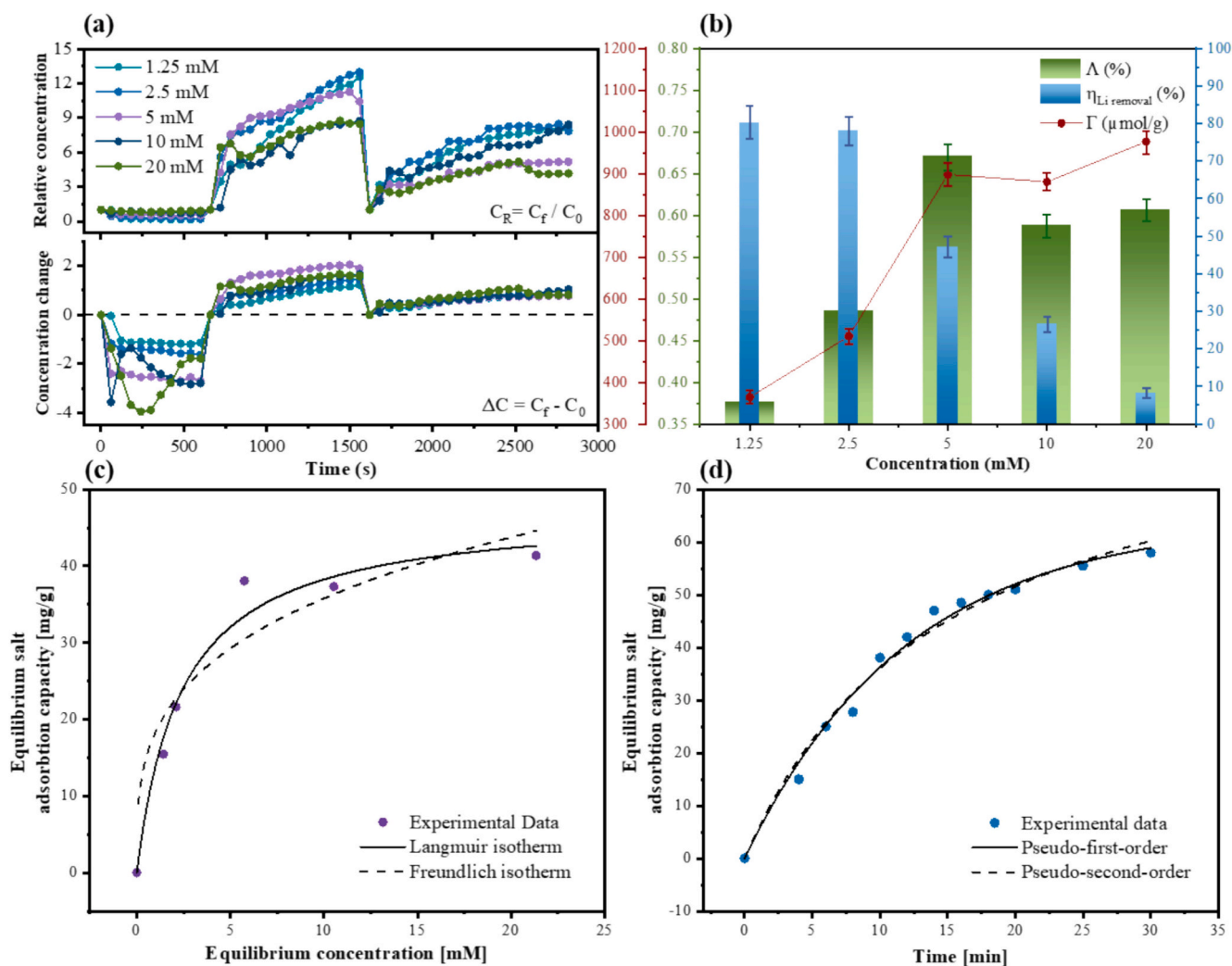


Fig. 12. Charge/discharge performance of the LMO/LAO mixed electrode in the MCDI Li capturing system with LiCl feed concentrations of 1.25 mM, 2.5 mM, 5 mM, 10 mM, and 20 mM, featuring: (a) Profiles of relative concentration [C_R] and change in concentration [ΔC]. (b) Performance metrics including Li⁺ adsorption amount [Γ], charge efficiency % [Λ], and Li removal efficiency % [η_{Li removal}]. (c) Electrodesorption isotherms. (d) Electrodesorption kinetics for the LMO/LAO mixed electrode.

where q_e (mg/g of active material) is the equilibrium amount of LiCl adsorbed/intercalated at the surface of the electrode and is calculated using Eq. (2), q_m (mg/g) denotes the maximum electrosorption capacity for monolayer coverage, and C_e (mg/L) is the equilibrium concentration of LiCl. K_L (L/mg) serves as the Langmuir constant which is associated with the enthalpy/heat of adsorption, while K_F (L/g) and n are constants from the Freundlich isotherm, where $1/n$ (ranging from 0 to 1) indicates the adsorption tendency of the adsorbate.

The Langmuir model assumes monolayer adsorption with no interaction between adsorbed species, ideal for evaluating heterogeneity in adsorption energies. Conversely, the Freundlich model accommodates surface heterogeneity and multilayer adsorption [57].

The values of various parameters and correlation coefficients for both isotherms are summarized in Table 3. According to Fig. 12c, these isotherm models exhibit strong correlation with the experimental data from the LMO/LAO-based electrode. The Langmuir isotherm suggests a maximum monolayer coverage (q_m) of 47.4 mg/g, indicating homogeneous adsorption energies across the electrosorption sites, while the Freundlich isotherm yields an n value >1 , implying favorable ion electrosorption conditions. A closer examination of the correlation coefficient (R^2) reveals that the electrosorption data align more closely with the Langmuir model. This fit suggests that Li adsorption onto the LMO/LAO electrode predominantly occurs as monolayer coverage. Although the Langmuir model was originally developed for organic and inorganic adsorption involving physical or chemical bonds on activated carbon [58], it proves effective here for describing electrosorption. In this process, ions adhere to the charged electrode surface through electrostatic interactions, similar to typical adsorption dynamic, affirming the suitability of the Langmuir model for characterizing these interactions.

The kinetics of the fabricated electrode were also studied through a series of experiments in the MCDI cell using 5 mM LiCl solution over various charge/discharge intervals. These experiments were analyzed using pseudo-first-order (Eq. (14)) and pseudo-second-order (Eq. (15)) adsorption kinetic models. The results, along with model-fitted plots and parameters, are presented in Fig. 12d and Table 3. The equations for pseudo-first-order and pseudo-second-order models are as follows:

$$\log(q_e - q) = \log q_e - \frac{k_1 t}{2.303} \quad (14)$$

$$\frac{t}{q} = \frac{1}{k_2 q_e^2} + \frac{t}{q_e} \quad (15)$$

where, q_e and q (mg/g) are the amount of LiCl adsorbed at equilibrium and time t (min), respectively, k_1 and k_2 are the adsorption rate constants for the pseudo-first-order and the pseudo-second-order models, respectively.

According to Fig. 12d, the equilibrium salt adsorption capacity is observed to increase with the duration of the charge/discharge cycles.

Table 3

Parameters determined by fitting experimental data into Langmuir and Freundlich isotherms, and pseudo-first-order and pseudo-second-order kinetic models for the MCDI performance of the LMO/LAO electrode.

	Equation	Parameters	Value
Langmuir isotherm model	$q_e = \frac{q_m K_L C_e}{1 + K_L C_e}$	q_m	47.428
		K_L	0.4172
		R^2	0.9774
		K_F	18.362
Freundlich isotherm model	$q_e = K_F C_e^{1/n}$	n	3.4496
		R^2	0.8215
		q_e	64.146
Pseudo-first-order kinetics model	$\log(q_e - q) = \log q_e - \frac{k_1 t}{2.303}$	k_1	0.0014
		R^2	0.9886
		q_e	90.675
		k_2	1.2134
Pseudo-second-order kinetics model	$\frac{t}{q} = \frac{1}{k_2 q_e^2} + \frac{t}{q_e}$	R^2	0.9829

The correlation coefficients for both models suggest they are effective in describing the experimental data, yet, the pseudo-first-order model shows a notably stronger fit, suggesting it more accurately reflects the adsorption kinetics observed in these experiments.

3.3.4. Effect of competing ions on Li⁺ recovery

A series of experiments evaluated the Li⁺ selectivity of the mixed LMO/LAO electrode using 5 mM single-salt solutions of LiCl, NaCl, KCl, MgCl₂, and CaCl₂. Fig. 13 displays the results, with Fig. 13a showing the charge/discharge curves in terms of ion adsorption amounts (Γ). Notably, Li⁺ exhibited the highest adsorption rate, reaching a peak of 900 $\mu\text{mol/g}$ at a rate of 32.4 $\mu\text{mol/g min}$ (Fig. 13b), with a preference order of Li⁺ $>$ Na⁺ $>$ Mg²⁺ $>$ Ca²⁺ $>$ K⁺ in terms of Γ , indicating that the LMO/LAO-CDI electrode has high selectivity to Li⁺. For specific SAC and SAR (Fig. 13b), Mg²⁺ followed Li⁺ closely with values of 20.58 mg/g and 2.05 mg/g min, respectively. However, regarding charge efficiency, Ca²⁺ had a slightly lower value than K⁺, reversing their positions from the previous Γ order.

Fig. 13c presents the separation factor ($\alpha_{M^{n+}}^{Li^+}$) for the electrode against various tested ions. Notably, the highest selectivity for Li ions was observed against K⁺, with a $\alpha_{K^+}^{Li^+}$ value nearing 40, correlating with the lowest salt adsorption of 70.37 $\mu\text{mol/g}$. This selectivity is attributed to the electrode's design, which optimizes confined void spaces particularly suited for Li, making it restrictive for larger ions like potassium. On the other hand, the electrode's selectivity for Li against Na⁺, Ca²⁺, and Mg²⁺ showed competitive behavior, with values of 5.74, 5.48, and 5.25, respectively. Among these, Mg²⁺ showed the most competitive behavior, exhibiting the highest adsorption capacity, salt adsorption rate, and charge efficiency but the lowest Li selectivity, likely due to its size similarity to Li⁺.

To assess the LMO/LAO mixed electrode's performance in conditions with higher concentrations of competing ions, its efficacy in recovering Li⁺ from synthetic brine (comprising 23.48 mM Li⁺, 120.83 mM Mg²⁺, 256.4 mM Na⁺, 47.83 mM K⁺, and 0.57 mM Ca²⁺ [59]) was investigated. Fig. 13d displays the adsorption results for various cations in the synthetic brine, revealing that Li⁺ adsorption reached 206 $\mu\text{mol/g}$, significantly surpassing Mg²⁺ (25 mmol/g), Na⁺ (60 mmol/g), K⁺ (8 mmol/g), and Ca²⁺ (0.6 mmol/g). These findings underscore the LMO/LAO mixed electrode's robust selectivity for Li⁺, validating its potential for Li extraction from real brine sources.

Further analysis explored the impact of co-existing Mg²⁺ on Li⁺ selectivity by measuring the separation factor ($\alpha_{Mg^{2+}}^{Li^+}$) at various Li⁺ to Mg²⁺ ratios (1:1, 1:2, and 1:5) within a 5 mM total concentration feed solution. The inset in Fig. 13d displays these values, showing a separation factor starting at about 5.24 at a 1:1 ratio and slightly increasing to 5.53 at a 1:5 ratio. This trend, consistent with previous studies [28,33,60], indicates that the substantial hydration radius and strong hydration energy of Mg²⁺ minimally affect Li intercalation [26], highlighting the electrode's effectiveness for Li extraction from solutions with a high Li to Mg ratio.

Table 4 further investigates the Li⁺ selectivity against Mg²⁺ by presenting the $\alpha_{Mg^{2+}}^{Li^+}$ values from various studies focused on this metric in MCDI systems. The table lists the type of electrodes tested, the initial ionic concentrations used, and the $\alpha_{Mg^{2+}}^{Li^+}$ at the most commonly evaluated 1:1 Li⁺ to Mg²⁺ molar ratio. The highest $\alpha_{Mg^{2+}}^{Li^+}$ of 9.2 was achieved using pure LMO material at a relatively high initial LiCl/MgCl₂ concentration of about 34.37 mM [14], although the associated salt adsorption capacity (SAC) was relatively low at 2.42 mg/g.

A clear relationship is evident between the initial concentration of the LiCl/MgCl₂ mixture and the achieved $\alpha_{Mg^{2+}}^{Li^+}$. As the initial concentration increases, so too does the selectivity for Li⁺ over Mg²⁺. This trend prompts concerns about the practicability of using highly concentrated feed solutions in natural Li-bearing liquid sources. For instance,

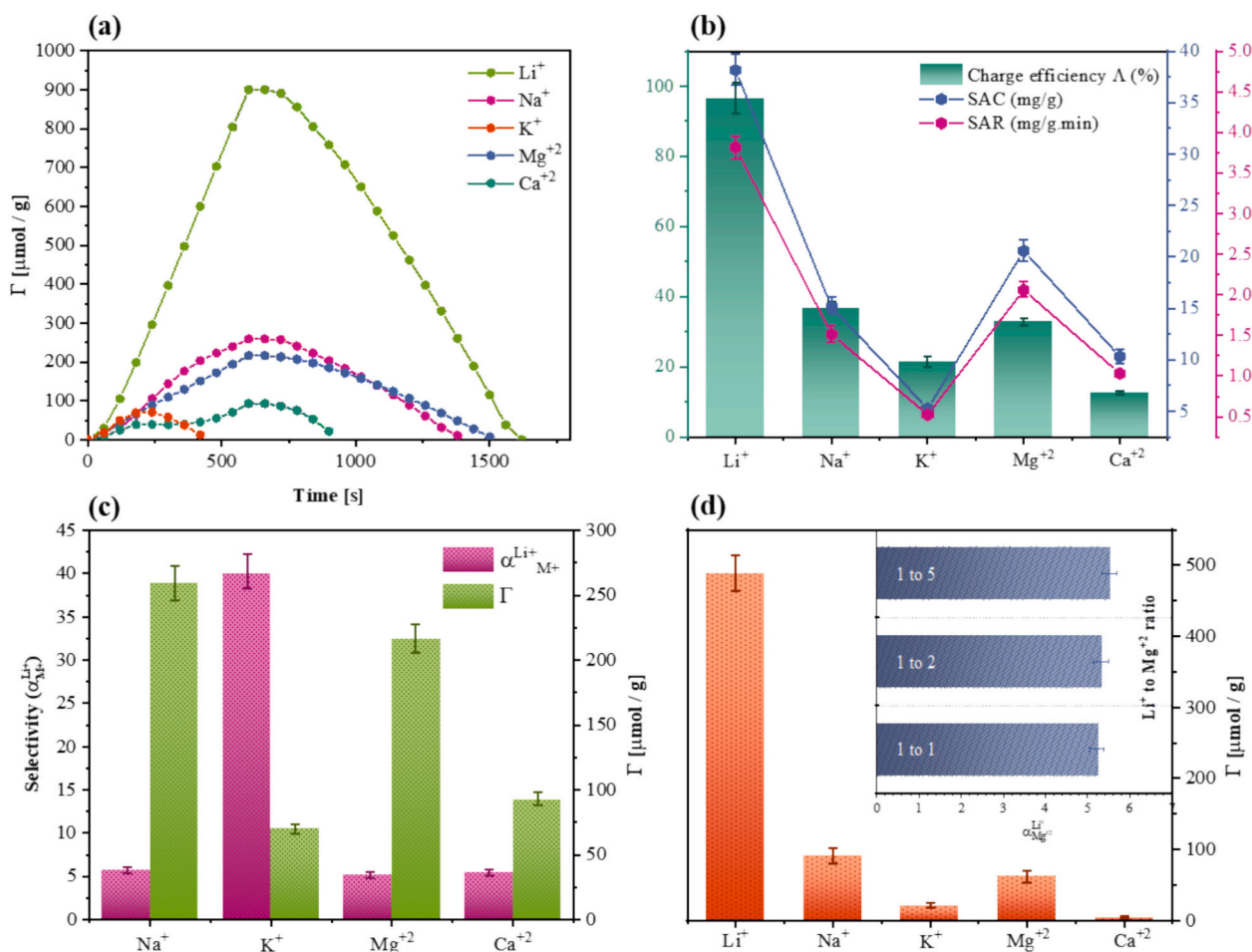


Fig. 13. Effect of competing ions on Li^+ adsorption in an MCDI cell using the LMO/LAO-CDI electrode with 5 mM single-salt solutions including LiCl, NaCl, KCl, MgCl_2 , and CaCl_2 , showing: (a) Adsorption amount $[\Gamma]$ for each ion, (b) Charge efficiency $[\Lambda]$, salt adsorption capacity [SAC], and salt adsorption rate [SAR] for various ions, (c) Separation factors of Li^+ relative to other ions ($\alpha_{M^+}^{\text{Li}^+}$). (d) Adsorption amounts of various ions in synthetic brine, along with $\alpha_{Mg^{2+}}^{\text{Li}^+}$ values at different Li^+ to Mg^{2+} ratios.

Table 4

Comparative analysis of Li recovery in MCDI processes focused on selectivity ($\alpha_{Mg^{2+}}^{\text{Li}^+}$).

Active cathode material	Initial salt conc. (mM)	Flow rate (ml/min)	SAC (mg/g)	$\alpha_{Mg^{2+}}^{\text{Li}^+}$	Li: Mg Mol ratio	year	Ref.
LMO	34.37	20	2.415	9.2	1:1	2017	[14]
LMO/GO	10	10	30.53	7	1:1	2023	[29]
MnO_2 /rGO	10	10	25.47	6.8	1:1	2022	[28]
LMO/LAO	5	10	38.15	5.25	1:1	2024	This study
LNMO	5	10	1.66	5.2	1:1	2021	[21]
LCMO	10	10	30.53	3.5	1:1	2023	[26]
AC w/ MSCDI	3.5996	10	-	2.95	1:1	2019	[13]
λ - MnO_2 sieve	10	10	33.9	0.583	1:1	2021	[17]
AC/ZIF-8-PDA	10	20	3	0.28	n.a.	2023	[33]

geothermal brines typically contain Li concentrations between 10 and 20 mg/L (1.44–2.88 mM) [9], while seawater holds vast Li reserves estimated at 230 billion tons [61] but features a very low Li concentration of about 0.17 mg/L [3]. Concentrations in seawater reverse

osmosis (SWRO) brines typically range from about 0.2 mg/L to 0.3 mg/L [62], emphasizing the challenge of achieving high selectivity and SAC in MCDI systems when handling complex feed solutions at lower concentrations. As a result, recent studies have aimed to reduce the initial concentrations to around 10 mM, still maintaining effective $\alpha_{Mg^{2+}}^{\text{Li}^+}$ and SAC levels. For example, employing graphene oxide (GO) treated LMO at an initial concentration of 10 mM led to a high SAC of 30.53 mg/g and a selectivity of 7.0 [29].

Addressing the challenge of lower feed concentrations, this study used an initial 5 mM LiCl/ MgCl_2 mixture, achieving a respectable $\alpha_{Mg^{2+}}^{\text{Li}^+}$ of 5.25. Although this is slightly lower than values from studies using 10 mM, it remains comparable given the 50% reduction in initial concentration. Similarly, an LNMO electrode [21] used in MCDI with a 5 mM initial concentration exhibited a selectivity of about 5.2 but a much lower SAC of around 1.66 mg/g. In contrast, this study reached an SAC of 38.15 mg/g, significantly enhancing the overall performance of Li recovery.

3.3.5. Stability of LMO/LAO mixed electrode in MCDI

The stability of the LMO/LAO mixed electrode was examined through 20 consecutive charge/discharge cycles in an MCDI setup using a 5 mM LiCl solution. Fig. 14a displays the current-time profiles of these cycles, which indicate minimal decay in capacitive performance. This slight degradation may be due to natural blocking or fouling by contaminants and precipitated salts, which can obscure active sites on the

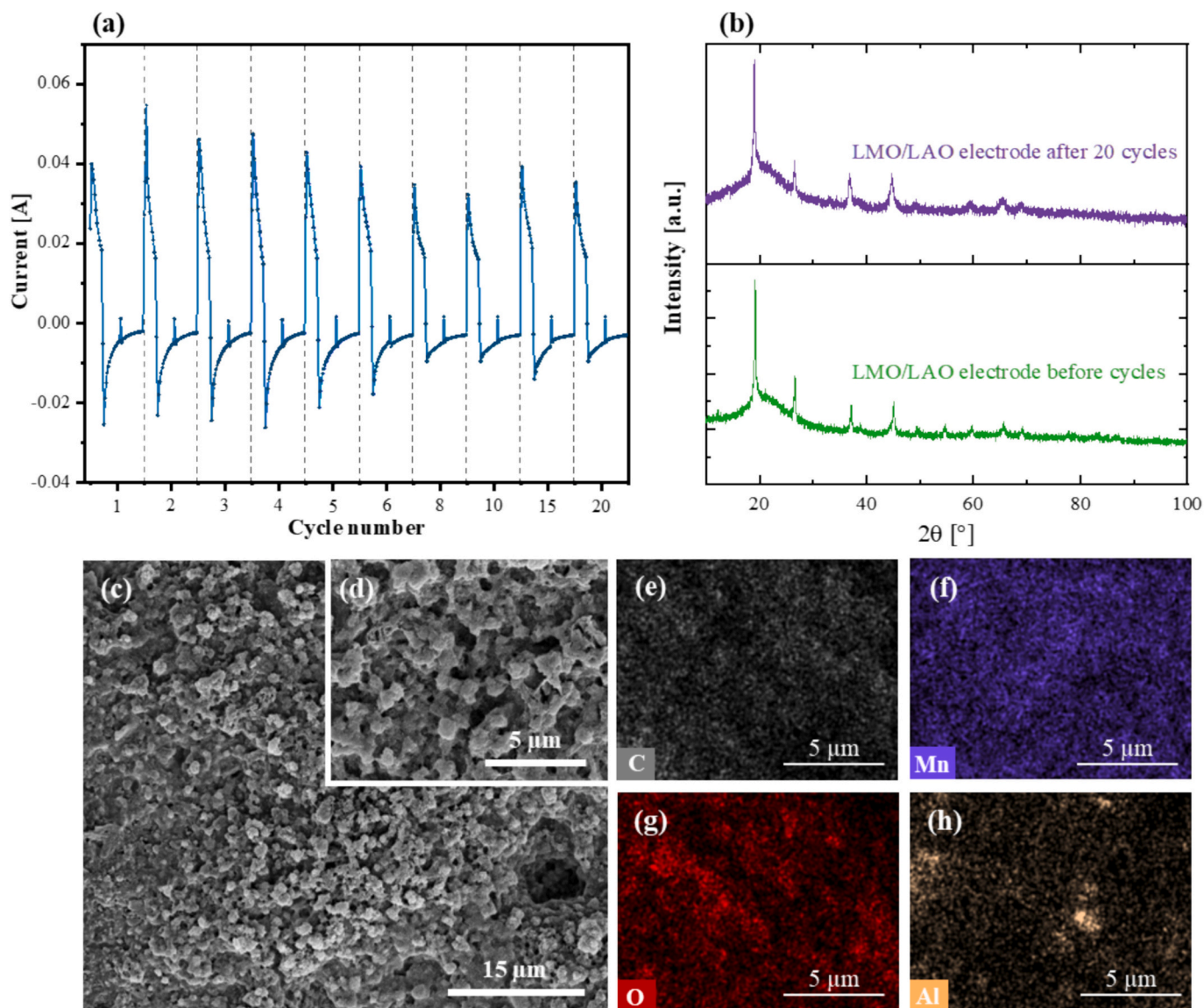


Fig. 14. (a) Cyclic performance of the LMO/LAO mixed electrode in MCDI using a 5 mM LiCl solution. (b) XRD spectra of the LMO/LAO mixed electrode before and after 20 charge/discharge cycles. (c and d) SEM image of LMO/LAO mixed electrode after 20 consecutive cycles. EDS elemental mapping of C (e), Mn (f), O (g), and Al (h).

electrode's surface and reduce its ion adsorption capacity in subsequent cycles. Nevertheless, XRD analysis of the fabricated electrode before and after 20 cycles reveals a stable crystalline structure without significant changes (Fig. 14b), indicating that the volume changes associated with Li^+ insertion and de-insertion are reversible. Additionally, SEM images of the electrode post-testing, including after exposure to simulated brine solution, confirm its structural stability with negligible morphological alterations. As depicted in Fig. 14c, the compact structure of the electrode remains intact, showing no visible degradation of its LMO and LAO components. Elemental mapping of key constituents (Mn, Al, C, O) further corroborates this finding, as shown in Fig. 14 e–h, highlighting the electrode's resilience and potential for long-term operational stability in MCDI applications.

4. Conclusion

This study explored the development of new and efficient electrodes for elemental Li recovery, investigating the potential applicability of a comprehensive Li recovery and recycling system to enhance the circular economy of Li. Selective Li intercalating electrodes were fabricated

using simulated spent Li-ion battery (SLiB) cathode materials based on $\text{LiMn}_2\text{O}_4/\text{LiAlO}_2$ mixtures. These electrodes were employed in a membrane-based capacitive deionization (MCDI) system for the selective recovery of Li. The main conclusions from this study include:

- XRD, XPS, and SEM analyses confirmed the successful fabrication of phase-pure de-lithiated LiMn_2O_4 (LMO) and LiAlO_2 (LAO) active cathode materials.
- Various cathodes with different LMO to LAO ratios were synthesized, and electrochemical assessments via CV, GCD, and EIS tests showed improved performance and specific capacitance, particularly with 10 % LAO incorporated into LMO. The LMO/LAO (90/10) electrode exhibited the longest discharge time of 290 s, indicating the highest specific capacitance (159.6 F/g) among the electrodes tested.
- In the MCDI system, the charge/discharge performance of the LMO/LAO (90/10) electrode achieved the highest adsorption capacity of $900 \mu\text{mol/g}$, outperforming LMO and AC electrodes, which recorded capacities of $365.0 \mu\text{mol/g}$ and $57.7 \mu\text{mol/g}$, respectively.
- The inclusion of 10 % LAO to 90 % LMO resulted in a substantial enhancement of about 146 % in specific adsorption capacity (SAC)

and salt adsorption rate (SAR), reaching values of 38.15 mg/g and 90.0 $\mu\text{mol/g}\cdot\text{min}$, respectively. The mixed electrode demonstrated superior performance metrics, including a charge efficiency of 96.5 %, a Li removal efficiency of 67 %, and a high discharge efficiency of around 83.13 %.

- The improved charge/discharge performance of the mixed LMO/LAO electrode is attributed to the LAO's contribution to forming a porous structure that enhances Li ion diffusion, accelerates intercalation/de-intercalation processes, and reduces internal resistance through the conductive properties of aluminum oxide.
- The LMO/LAO-CDI electrode demonstrated substantial selectivity for Li^+ , with an adsorption rate of 720.2 $\mu\text{mol/g}$, significantly higher than other competing ions, confirming a preference order of $\text{Li}^+ > \text{Na}^+ > \text{Mg}^{2+} > \text{Ca}^{2+} > \text{K}^+$. The study also highlighted the minimal impact of Mg^{2+} on Li^+ intercalation, emphasizing the electrode's efficacy for selective Li extraction from sources with a high $\text{Mg}^{2+}/\text{Li}^+$ ratio.
- Comparative analysis with previous research on MCDI Li^+ capture systems indicated that the LMO/LAO mixed electrode surpassed other studies within the tested concentration range. Moreover, compared to previous CDI studies, the system maintained a low specific energy consumption of 0.67 kWh/m^3 .

Author statement

Tasneem Elmakki: Conceptualization, Investigation, Methodology, Visualization, Writing- Original draft preparation.: **Sifani Zavahir:** Data curation, Investigation, Writing- Original draft preparation.: **Ho Kyong Shon:** Conceptualization, Writing- review & editing.: **Guillermo Hijos Gago:** Investigation, Writing- review & editing.: **Hyunwoong Park:** Investigation, Writing- review & editing.: **Dong Suk Han:** Conceptualization, Data curation, Investigation, Funding acquisition, Supervision, Writing- Reviewing and Editing.

Declaration of competing interest

The authors declare that they have no known competing financial interests or personal relationships that could have appeared to influence the work reported in this paper. Ho Kyong Shon serves as an Editor-in-Chief for the journal, while the editorial handling and review of this manuscript were overseen by a different Editor-in-Chief.

Acknowledgment

This project is supported by the International Research Collaboration Co-Fund (IRCC)(# IRCC-2024-364) of Qatar University and Australian Research Council (ARC) through the ARC Research Hub for Nutrients in a Circular Economy (NiCE) (IH210100001). H.P. is grateful to the National Research Foundation of Korea (RS-2023-00254645) and the Technology Innovation Program (20032599) funded by the Ministry of Trade Industry & Energy, Korea.

Data availability

Data will be made available on request.

References

- [1] P. Waengwan, T. Eksangsi, Recovery of lithium from simulated secondary resources (LiCO_3) through solvent extraction, *Sustainability* 12 (2020) 7179.
- [2] L.-F. Zhou, D. Yang, T. Du, H. Gong, W.-B. Luo, The current process for the recycling of spent lithium ion batteries, *Front. Chem.* 8 (2020) 578044.
- [3] A. Siekierka, E. Kmiecik, B. Tomaszewska, K. Wator, M. Bryjak, The evaluation of the effectiveness of lithium separation by hybrid capacitive deionization from geothermal water with the uncertainty measurement application, *Desalin. Water Treat.* 128 (2018) 259–264.
- [4] A.M. Salces, N. Kelly, G.J. Streblov, E.T. Temel, M. Rudolph, A. Chagnes, A. Vanderbruggen, A contribution to understanding ion-exchange mechanisms for lithium recovery from industrial effluents of lithium-ion battery recycling operations, *J. Environ. Chem. Eng.* 12 (2024) 112951.
- [5] J. Sun, X. Li, Y. Huang, G. Luo, D. Tao, J. Yu, L. Chen, Y. Chao, W. Zhu, Preparation of high hydrophilic H_2TiO_3 ion sieve for lithium recovery from liquid lithium resources, *Chem. Eng. J.* 453 (2023) 139485.
- [6] M.R. Mojid, K.J. Lee, J. You, A review on advances in direct lithium extraction from continental brines: ion-sieve adsorption and electrochemical methods for varied mg/Li ratios, *Sustain. Mater. Technol.* 40 (2024) e00923.
- [7] D.Y. Butylskii, V. Troitskiy, N. Smirnova, N. Pismenskaya, Y. Wang, C. Jiang, T. Xu, V. Nikonenko, Review of recent progress on lithium recovery and recycling from primary and secondary sources with membrane-based technologies, *Desalination* 117826 (2024).
- [8] S.-L. Gao, Z.-X. Qin, B.-F. Wang, J. Huang, Z.-L. Xu, Y.-J. Tang, Lithium recovery from the spent lithium-ion batteries by commercial acid-resistant nanofiltration membranes: a comparative study, *Desalination* 572 (2024) 117142.
- [9] S. Zavahir, T. Elmakki, M. Gulied, Z. Ahmad, L. Al-Sulaiti, H.K. Shon, Y. Chen, H. Park, B. Batchelor, D.S. Han, A review on lithium recovery using electrochemical capturing systems, *Desalination* 500 (2021) 114883.
- [10] A. Battistel, M.S. Palagonia, D. Brogioli, F. La Mantia, R. Tricoli, Electrochemical methods for lithium recovery: a comprehensive and critical review, *Adv. Mater.* 32 (2020) 1905440.
- [11] P. Srimuk, X. Su, J. Yoon, D. Aurbach, V. Presser, Charge-transfer materials for electrochemical water desalination, ion separation and the recovery of elements, *Nat. Rev. Mater.* 5 (2020) 517–538.
- [12] E. Avraham, B. Shapira, I. Cohen, D. Aurbach, Electrical double layer in nano-pores of carbon electrodes: beyond CDI; sensing and maximizing energy extraction from salinity gradients, *Curr. Opin. Electrochem.* 36 (2022) 101107.
- [13] W. Shi, X. Liu, C. Ye, X. Cao, C. Gao, J. Shen, Efficient lithium extraction by membrane capacitive deionization incorporated with monovalent selective cation exchange membrane, *Sep. Purif. Technol.* 210 (2019) 885–890.
- [14] D.-H. Lee, T. Ryu, J. Shin, J.C. Ryu, K.-S. Chung, Y.H. Kim, Selective lithium recovery from aqueous solution using a modified membrane capacitive deionization system, *Hydrometallurgy* 173 (2017) 283–288.
- [15] T. Ryu, J.C. Ryu, J. Shin, D.H. Lee, Y.H. Kim, K.-S. Chung, Recovery of lithium by an electrostatic field-assisted desorption process, *Ind. Eng. Chem. Res.* 52 (2013) 13738–13742.
- [16] T. Ryu, D.-H. Lee, J.C. Ryu, J. Shin, K.-S. Chung, Y.H. Kim, Lithium recovery system using electrostatic field assistance, *Hydrometallurgy* 151 (2015) 78–83.
- [17] B. Kim, J.Y. Seo, C.-H. Chung, Electrochemical desalination and recovery of lithium from saline water upon operation of a capacitive deionization cell combined with a redox flow battery, *ACS ES&T Water* 1 (2021) 1047–1054.
- [18] S. Bae, S.-i. Jeon, W. Lee, Y. Kim, K. Cho, Four-step constant voltage operation of hybrid capacitive deionization with composite electrodes for bifunctional deionization and lithium recovery, *Desalination*, 565 (2023) 116883.
- [19] Y. Jiang, K. Li, S.I. Alhassan, Y. Cao, H. Deng, S. Tan, H. Wang, C. Tang, L. Chai, Spinel LiMn_2O_4 as a capacitive deionization electrode material with high desalination capacity: experiment and simulation, *Int. J. Environ. Health Res.* 20 (2022) 517.
- [20] A. Siekierka, Lithium iron manganese oxide as an adsorbent for capturing lithium ions in hybrid capacitive deionization with different electrical modes, *Sep. Purif. Technol.* 236 (2020) 116234.
- [21] X. Shang, B. Hu, P. Nie, W. Shi, T. Hussain, J. Liu, $\text{LiNi}_{0.5}\text{Mn}_{1.5}\text{O}_4$ -based hybrid capacitive deionization for highly selective adsorption of lithium from brine, *Sep. Purif. Technol.* 258 (2021) 118009.
- [22] A. Siekierka, M. Bryjak, Selective sorbents for recovery of lithium ions by hybrid capacitive deionization, *Desalination* 520 (2021) 115324.
- [23] A. Siekierka, Lithium and magnesium separation from brines by hybrid capacitive deionization, *Desalination* 527 (2022) 115569.
- [24] X. Zhao, G. Li, M. Feng, Y. Wang, Semi-continuous electrochemical extraction of lithium from brine using CF-NMMO/AC asymmetric hybrid capacitors, *Electrochim. Acta* 331 (2020) 135285.
- [25] X. Shang, Z. Liu, W. Ji, H. Li, Synthesis of lithium vanadate/reduced graphene oxide with strong coupling for enhanced capacitive extraction of lithium ions, *Sep. Purif. Technol.* 262 (2021) 118294.
- [26] B. Hu, B. Zhang, Y. Wang, M. Li, J. Yang, J. Liu, Prussian blue analogue derived 3D hollow LiCoMnO_4 nanocube for selective extraction of lithium by pseudo-capacitive deionization, *Desalination* 560 (2023) 116662.
- [27] Y. Sun, Z. Liu, X. Chen, X. Yang, F. Xiang, W. Lu, Enhancing the stabilities and electrochemical performances of $\text{LiNi}_{0.5}\text{Co}_{0.2}\text{Mn}_{0.3}\text{O}_2$ cathode material by simultaneous LiAlO_2 coating and Al doping, *Electrochim. Acta* 376 (2021) 138038.
- [28] B. Hu, X. Shang, P. Nie, B. Zhang, J. Yang, J. Liu, Lithium ion sieve modified three-dimensional graphene electrode for selective extraction of lithium by capacitive deionization, *J. Colloid Interface Sci.* 612 (2022) 392–400.
- [29] J. Yang, X. Shang, B. Hu, B. Zhang, Y. Wang, J. Yang, J. Liu, In situ growth of LiMn_2O_4 on graphene oxide for efficient lithium extraction by capacitive deionization, *J. Solid State Electrochem.* (2023) 1–9.
- [30] W. Jin, M. Hu, Z. Sun, C.-H. Huang, H. Zhao, Simultaneous and precise recovery of lithium and boron from salt lake brine by capacitive deionization with oxygen vacancy-rich $\text{CoP}/\text{Co}_3\text{O}_4$ -graphene aerogel, *Chem. Eng. J.* 420 (2021) 127661.
- [31] Y. Ha, H.B. Jung, H. Lim, P.S. Jo, H. Yoon, C.-Y. Yoo, T.K. Pham, W. Ahn, Y. Cho, Continuous lithium extraction from aqueous solution using flow-electrode capacitive deionization, *Energies* 12 (2019) 2913.
- [32] A. Siekierka, M. Bryjak, Novel anion exchange membrane for concentration of lithium salt in hybrid capacitive deionization, *Desalination* 452 (2019) 279–289.
- [33] H. Yu, S.M. Hossain, C. Wang, Y. Choo, G. Naidu, D.S. Han, H.K. Shon, Selective lithium extraction from diluted binary solutions using metal-organic frameworks

- (MOF)-based membrane capacitive deionization (MCDI), *Desalination* 556 (2023) 116569.
- [34] C. Tomon, S. Sarawutanukul, N. Phattharasupakun, S. Duangdangchote, P. Chomkhuntod, N. Joraleechanchai, P. Bunyanidhi, M. Sawangphruk, Core-shell structure of LiMn_2O_4 cathode material reduces phase transition and Mn dissolution in Li-ion batteries, *Commun. Chem* 5 (2022) 54.
- [35] H. Zou, B. Wang, F. Wen, L. Chen, Hydrothermal synthesis of pure LiMn_2O_4 from nanostructured MnO_2 precursors for aqueous hybrid supercapacitors, *Ionics* 23 (2017) 1083–1090.
- [36] T. Elmakki, S. Zavahir, U. Hafsa, L. Al-Sulaiti, Z. Ahmad, Y. Chen, H. Park, H. K. Shon, Y.-C. Ho, D.S. Han, Novel LiAlO_2 material for scalable and facile lithium recovery using electrochemical ion pumping, *Nanomaterials* 13 (2023) 895.
- [37] T. Zhang, D. Li, Z. Tao, J. Chen, Understanding electrode materials of rechargeable lithium batteries via DFT calculations, *Prog. Nat. Sci.: Mater. Int.* 23 (2013) 256–272.
- [38] L. Wei, S.-X. Zhao, X. Wu, S.-J. Zhao, C.-W. Nan, The existence form and synergistic effect of P in improving the structural stability and electrochemical performance of $\text{Li}_2\text{Mn}_{0.5}\text{Fe}_{0.5}\text{SiO}_4/\text{C}$ cathode materials, *J. Mater.* 4 (2018) 179–186.
- [39] B. Hu, Y. Wang, X. Shang, K. Xu, J. Yang, M. Huang, J. Liu, Structure-tunable $\text{Mn}_3\text{O}_4\text{-Fe}_3\text{O}_4/\text{C}$ hybrids for high-performance supercapacitor, *J. Colloid Interface Sci.* 581 (2021) 66–75.
- [40] Y. Wu, Y.-F. Li, L.-Y. Wang, Y.-J. Bai, Z.-Y. Zhao, L.-W. Yin, H. Li, Enhancing the Li-ion storage performance of graphite anode material modified by LiAlO_2 , *Electrochim. Acta* 235 (2017) 463–470.
- [41] R.-C. Fang, Q.-Q. Sun, P. Zhou, W. Yang, P.-F. Wang, D.W. Zhang, High-performance bilayer flexible resistive random access memory based on low-temperature thermal atomic layer deposition, *Nanoscale Res. Lett.* 8 (2013) 1–7.
- [42] T.-F. Yi, Y. Li, Z. Fang, P. Cui, S. Luo, Y. Xie, Improving the cycling stability and rate capability of $\text{LiMn}_{0.5}\text{Fe}_{0.5}\text{PO}_4/\text{C}$ nanorod as cathode materials by LiAlO_2 modification, *J. Mater.* 6 (2020) 33–44.
- [43] J.S. Park, X. Meng, J.W. Elam, S. Hao, C. Wolverton, C. Kim, J. Cabana, Ultrathin lithium-ion conducting coatings for increased interfacial stability in high voltage lithium-ion batteries, *Chem. Mater.* 26 (2014) 3128–3134.
- [44] J. Abou-Rjeily, I. Bezza, N.A. Laziz, C. Autret-Lambert, M.T. Sougrati, F. Ghamouss, High-rate cyclability and stability of LiMn_2O_4 cathode materials for lithium-ion batteries from low-cost natural $\beta\text{-MnO}_2$, *Energy Storage Mater.* 26 (2020) 423–432.
- [45] Q. Song, Y. Wen-Ning, W. Li, C.C. Lian-Shan ZHANG, M. Li-Juan, M. Shi-Gang, Facile synthesis of $\text{Si}@ \text{LiAlO}_2$ nanocomposites as anode for lithium-ion battery, *Chin. J. Ino. Chem.* 38 (2022) 1655–1662.
- [46] J. Zhang, J. Shen, C. Wei, H. Tao, Y. Yue, Synthesis and enhanced electrochemical performance of the honeycomb $\text{TiO}_2/\text{LiMn}_2\text{O}_4$ cathode materials, *J. Solid State Electrochem.* 20 (2016) 2063–2069.
- [47] J. Fan, L.-L. Yu, G.-D. Fan, W.-L. Xu, J.-J. Xing, J.-T. Zhao, Cubic nanocrystal constructed 3D porous LiMn_2O_4 : low-temperature pyrolysis formation and high-performance as a cathode material for aqueous hybrid capacitor, *J. Mater.* 7 (2021) 488–497.
- [48] H. Joo, J. Lee, J. Yoon, Short review: timeline of the electrochemical lithium recovery system using the spinel LiMn_2O_4 as a positive electrode, *Energies* 13 (2020) 6235.
- [49] J. Gao, S. Shi, R. Xiao, H. Li, Synthesis and ionic transport mechanisms of $\alpha\text{-LiAlO}_2$, *Solid State Ion.* 286 (2016) 122–134.
- [50] L. Cheng, Interface Engineering of Garnet Solid Electrolytes, University of California, Berkeley, 2015.
- [51] P. Wakudkar, A. Deshpande, Enhancement of ionic conductivity by addition of LiAlO_2 in $\text{Li}_{6.6}\text{La}_3\text{Zr}_{1.6}\text{Sb}_{0.4}\text{O}_{12}$ for lithium ion battery, *Solid State Ion.* 345 (2020) 115185.
- [52] M.M. Islam, T. Bredow, Interstitial lithium diffusion pathways in $\gamma\text{-LiAlO}_2$: a computational study, *J. Phys. Chem. Lett.* 6 (2015) 4622–4626.
- [53] K. Jo, Y. Baek, C. Lee, J. Yoon, Effect of hydrophilicity of activated carbon electrodes on desalination performance in membrane capacitive deionization, *Appl. Sci.* 9 (2019) 5055.
- [54] C. Santos, J.J. Lado, E. Garcia-Quismondo, J. Soria, J. Palma, M.A. Anderson, Maximizing volumetric removal capacity in capacitive deionization by adjusting electrode thickness and charging mode, *J. Electrochem. Soc.* 165 (2018) E294.
- [55] W. Tang, Z. Chen, H. Huang, M. Irfan, C. Huang, Z. Yang, W. Zhang, PVP-bridged $\gamma\text{-LiAlO}_2$ nanolayer on $\text{Li}_{1.2}\text{Ni}_{0.182}\text{Co}_{0.08}\text{Mn}_{0.538}\text{O}_2$ cathode materials for improving the rate capability and cycling stability, *Chem. Eng. Sci.* 229 (2021) 116126.
- [56] T.-H. Chen, K.-H. Yeh, C.-F. Lin, M. Lee, C.-H. Hou, Technological and economic perspectives of membrane capacitive deionization (MCDI) systems in high-tech industries: from tap water purification to wastewater reclamation for water sustainability, *Resour. Conserv. Recycl.* 177 (2022) 106012.
- [57] Y. Wimalasiri, M. Mossad, L. Zou, Thermodynamics and kinetics of adsorption of ammonium ions by graphene laminate electrodes in capacitive deionization, *Desalination* 357 (2015) 178–188.
- [58] K.Y. Foo, B.H. Hameed, Insights into the modeling of adsorption isotherm systems, *Chem. Eng. J.* 156 (2010) 2–10.
- [59] X. Zhao, M. Feng, Y. Jiao, Y. Zhang, Y. Wang, Z. Sha, Lithium extraction from brine in an ionic selective desalination battery, *Desalination* 481 (2020) 114360.
- [60] H. Saif, J. Crespo, S. Pawlowski, Lithium recovery from brines by lithium membrane flow capacitive deionization (Li-MFCDI)—a proof of concept, *JMS Lett.* 3 (2023) 100059.
- [61] H. Joo, S. Kim, S. Kim, M. Choi, S.-H. Kim, J. Yoon, Pilot-scale demonstration of an electrochemical system for lithium recovery from the desalination concentrate, *Environ. Sci.: Water Res.* 6 (2020) 290–295.
- [62] B. Swain, Recovery and recycling of lithium: a review, *Sep. Purif. Technol.* 172 (2017) 388–403.